Symmetry-Preserving Reduced-Order Wind Observers with Flight Test Results

Jeremy W. Hopwood*
Mississippi State University, Mississippi State, MS 39762

Benjamin M. Simmons† and Craig A. Woolsey‡
Virginia Tech, Blacksburg, VA 24061

Inferring wind velocity from aircraft motion is an enabling technology with applications in synthetic air data systems, path planning, safety monitoring, and atmospheric science. A reduced-order nonlinear state observer is developed to estimate wind velocity from aircraft motion. The observer is constructed by leveraging the symmetry of aircraft dynamics under the action of a Lie group to achieve global exponential convergence of the wind estimates to their true value. By only estimating the unmeasured wind and air-relative velocity, this reduced-order observer reduces computational complexity and simplifies nonlinear stability analysis. This approach eliminates the need for a small-perturbation assumption on the nonlinear dynamics yet casts the nonlinear wind estimation problem as the design of a linear, time-varying observer. Simulations and flight test results for a fixed-wing aircraft demonstrate the observer's performance and robustness to unmodeled turbulence, aerodynamic modeling error, and measurement noise, highlighting its practical applicability and potential to ensure safe operation of future aircraft systems.

I. Introduction

Inferring wind velocity from aircraft motion is an enabling technology across a wide range of applications. In aeronautics, wind estimates can be used in synthetic air data systems [1, 2] and path planning algorithms [3, 4]. Furthermore, having quantified the accuracy of wind estimates [5] and/or guaranteed their convergence [6], wind estimation algorithms can be incorporated into safety monitoring systems, such as those described in Refs. [7] and [8], to replace traditional measurement techniques. Closely tied to aviation, wind estimates are also vital to weather prediction and atmospheric science [9–12]. These areas of application have become intertwined, especially within the poorly sampled atmospheric boundary layer, with the emergence of small UAS and advances in the Urban/Advanced Air Mobility mission [13, 14]. For example, the development of wind estimation technologies is important in relaxing margins for flight safety to enable more weather-tolerant operations [15, 16].

The development of model-based wind estimation algorithms has brought finer temporal resolution and greater accuracy to wind velocity estimates [6, 17–19]. These *indirect* approaches feature a low instrumentation barrier as they do not require specialized sensors, such as an anemometer, to measure wind velocity. Instead, a model of the aircraft dynamics is used in conjunction with standard navigational sensors (e.g., accelerometer, gyroscope, magnetometer, and GNSS) to continuously estimate wind velocity at the aircraft's location.

The accuracy and stability guarantees of wind estimation approaches generally fall to the severity of approximations and assumptions made. Most common is the small-perturbation assumption that allows a linear flight dynamic model to be used with a linear state estimation scheme (e.g., the Kalman filter or H_∞ filter). Even approximate nonlinear filter techniques such as the extended Kalman filter (EKF) only retain their formal guarantees for small perturbations about steady motion with sufficiently low noise [20]. For aircraft, there are two ways in which the small-perturbation assumption may be violated. The first is aggressive maneuvering and agile flight — especially applicable for UAVs which do not impose the physiological limitations of the human pilot. The second is large changes in wind conditions as especially common in urban scenarios with the "urban canyon effect." Even if the vehicle is steadily translating in inertial space, the large changes to the flow condition necessitate a more careful approach in the nonlinear setting. This motivates the exploration of nonlinear observer techniques for wind estimation. In contrast to conventional state estimators, nonlinear observers provide stability guarantees on the dynamics of the state estimation error.

Model-based wind estimation methods that move beyond the small-perturbation assumption remain relatively limited. Nonetheless, several promising nonlinear approaches have emerged. One example is the nonlinear, passivity-based observer detailed in [6]. This approach uses the nonlinear aircraft dynamics in a passivity-based formulation [21] to construct an extended state observer that is globally exponentially stable provided the aerodynamics are not highly nonlinear (e.g., stall). Another approach to overcome the limitations of linear wind estimation is the invariant extended Kalman filter [22, 23], which is applicable to systems that are invariant under a Lie group's action (e.g., rigid body transformations). The invariant EKF is a type of local *symmetry-preserving* observer, which ensures the observer dynamics are invariant under the same Lie group action [24, 25]. It aims to expand the set of trajectories for which stability is assured by leveraging this symmetry. These so-called *permanent trajectories* are a generalization of steady motions for which convergence is guaranteed.

Typical approaches to model-based wind estimation produce

This is the accepted manuscript of an article published in the *Journal of Guidance, Control, and Dynamics*. The version of record is available at `https://doi.org/10.2514/1.G009281`.

estimates not only of wind velocity and air-relative velocity but also of measured states such as position, attitude, and angular velocity [26, 27]. Such full-order observers often re-estimate quantities that are already measured, adding unnecessary complexity. A natural alternative is to design a reduced-order observer [28], in which only the unmeasured portion of the state is estimated. However, reduced-order nonlinear observer design is non-constructive. This limitation has hindered the application of reduced-order nonlinear observers to many practical problems. In Ref. [29], the authors overcome this barrier by leveraging symmetries in a nonlinear system to construct a reduced-order observer. Here, we apply this theoretical framework to the wind estimation problem, where rotational symmetries in the aircraft equations of motion are leveraged to obtain an exponentially stable nonlinear observer.

The remainder of this paper is organized as follows. Section II presents the aircraft dynamics in wind and details how they are invariant under rotations. Next, Section III details the design of symmetry-preserving reduced-order observers for aircraft in wind from the perspective of two different reference frames. Section IV discusses aspects of practical implementation and tuning, followed by simulation and flight-test demonstrations using a fixed-wing aircraft in Section V. Concluding remarks are given in Section VII.

II. Invariant Aircraft Dynamics in Wind

A. Rigid-Body Kinematics

Consider an aircraft, modeled as a rigid body of mass m. Let the orthonormal vectors $\{\boldsymbol{i}_1, \boldsymbol{i}_2, \boldsymbol{i}_3\}$ define an earth-fixed North-East-Down (NED) reference frame, $\mathcal{F}_{\rm I}$, which we take to be inertial over the spatial and temporal scales of vehicle motion. Let the orthonormal vectors $\{\boldsymbol{b}_1, \boldsymbol{b}_2, \boldsymbol{b}_3\}$ define the body-fixed frame, $\mathcal{F}_{\rm B}$, centered at the aircraft center of gravity (CG) with $\boldsymbol{b}_1$ out the front of the aircraft, $\boldsymbol{b}_2$ out the right-hand side, and $\boldsymbol{b}_3$ pointing downward to complete a right-handed frame. The position of the body frame with respect to the inertial frame is given by the vector $\boldsymbol{q} = [x\ y\ z]^{\mathsf{T}} \in \mathbb{R}^3$. The attitude of the aircraft is described by the rotation matrix $\boldsymbol{R}_{\rm IB} \in \mathsf{SO}(3)$ that maps free vectors from $\mathcal{F}_{\rm B}$ to $\mathcal{F}_{\rm I}$. The aircraft's configuration is described by the point $(\boldsymbol{q}, \boldsymbol{R}_{\rm IB})$ in the special Euclidean group, $\mathsf{SE}(3) = \mathbb{R}^3 \rtimes \mathsf{SO}(3)$, where $\rtimes$ is the semi-direct product which expresses how two elements of the group compose a new element [30, §9.6]. Let $\boldsymbol{v} = [u\ v\ w]^{\mathsf{T}}$ and $\boldsymbol{\omega} = [p\ q\ r]^{\mathsf{T}}$ be the translational and rotational velocity of the aircraft with respect to $\mathcal{F}_{\rm I}$ expressed in $\mathcal{F}_{\rm B}$, respectively. The kinematic equations of motion are

$$\dot{\boldsymbol{q}} = \boldsymbol{R}_{\rm IB}\boldsymbol{v} \tag{1a}$$
$$\dot{\boldsymbol{R}}_{\rm IB} = \boldsymbol{R}_{\rm IB}\boldsymbol{S}(\boldsymbol{\omega}) \tag{1b}$$

where $\boldsymbol{S}(\cdot)$ is the skew-symmetric cross product equivalent matrix satisfying $\boldsymbol{S}(\boldsymbol{a})\boldsymbol{b} = \boldsymbol{a} \times \boldsymbol{b}$ for 3-vectors $\boldsymbol{a}$ and $\boldsymbol{b}$. Geometrically, these kinematics are defined on the tangent bundle $\mathsf{TSE}(3) = \bigcup_{\boldsymbol{p}\in\mathsf{SE}(3)} \mathsf{T}_{\boldsymbol{p}}\mathsf{SE}(3)$, where $\mathsf{T}_{\boldsymbol{p}}\mathsf{SE}(3)$ denotes the tangent space to $\mathsf{SE}(3)$ at the point $\boldsymbol{p} = (\boldsymbol{q}, \boldsymbol{R}_{\rm IB})$.

B. Dynamics in Steady and Uniform Wind

Since the aim is to estimate wind velocity, we now consider the aircraft dynamics in a time-varying wind field, $\boldsymbol{W} : \mathbb{R}^3 \times \mathbb{R} \to \mathbb{R}^3$, defined in the inertial frame. Let the instantaneous wind vector as experienced by the aircraft be

$$\boldsymbol{w}(t) = \boldsymbol{W}(\boldsymbol{q}(t), t) \tag{2}$$

The *apparent wind* $\boldsymbol{w}$ is taken to be part of the aircraft's *extended state*. The apparent wind along with the aircraft body velocity, $\boldsymbol{v}$, define the air-relative velocity in the body frame, $\boldsymbol{v}_{\rm r}$, via the *wind triangle*

$$\boldsymbol{v}_{\rm r} = \boldsymbol{v} - \boldsymbol{R}_{\rm IB}^{\mathsf{T}}\boldsymbol{w} \tag{3}$$

For the purpose of the observer design, we assume the following.

Assumption 1. *The wind field is uniform and steady on the space and time scales considered. In other words,* $\dot{\boldsymbol{w}} = \boldsymbol{0}$.

Under this assumption, the translational dynamics expressed in terms of air-relative velocity are

$$\dot{\boldsymbol{v}}_{\rm r} = \boldsymbol{v}_{\rm r} \times \boldsymbol{\omega} + \boldsymbol{R}_{\rm IB}^{\mathsf{T}}\boldsymbol{g} + \frac{1}{m}\boldsymbol{F} \tag{4}$$

where $\boldsymbol{F}$ is the body-frame aerodynamic force and $\boldsymbol{g}$ is the gravitational acceleration vector. Letting $\boldsymbol{I}$ be the body-frame moment of inertia matrix and $\boldsymbol{M}$ be the aerodynamic moment in the body frame, the rotational dynamics are

$$\dot{\boldsymbol{\omega}} = \boldsymbol{I}^{-1}\left(\boldsymbol{I}\boldsymbol{\omega} \times \boldsymbol{\omega} + \boldsymbol{M}\right) \tag{5}$$

To simplify the observer design, we make the following assumption on the aircraft's aerodynamics.

Assumption 2. *The aircraft's aerodynamic force and moment satisfy*

$$\boldsymbol{F} = \boldsymbol{F}_0 + \boldsymbol{F}_v\boldsymbol{v}_{\rm r} + \boldsymbol{F}_\omega\boldsymbol{\omega} \tag{6a}$$
$$\boldsymbol{M} = \boldsymbol{M}_0 + \boldsymbol{M}_v\boldsymbol{v}_{\rm r} + \boldsymbol{M}_\omega\boldsymbol{\omega} \tag{6b}$$

where $\boldsymbol{F}_{(\cdot)}$ *and* $\boldsymbol{M}_{(\cdot)}$ *are known signals.*

Equation (6) reflects a linearization of force and moment nonlinearities comprising the unknown air-relative velocity $\boldsymbol{v}_{\rm r}$. Practical considerations and consequences of Assumption 2 are discussed in Section IV.

Altogether, the aircraft equations of motion used for the observer design are

$$\dot{\boldsymbol{q}} = \boldsymbol{R}_{\rm IB}\boldsymbol{v}_{\rm r} + \boldsymbol{w} \tag{7a}$$
$$\dot{\boldsymbol{R}}_{\rm IB} = \boldsymbol{R}_{\rm IB}\boldsymbol{S}(\boldsymbol{\omega}) \tag{7b}$$
$$\dot{\boldsymbol{\omega}} = \boldsymbol{I}^{-1}\left(\boldsymbol{I}\boldsymbol{\omega} \times \boldsymbol{\omega} + \boldsymbol{M}_0 + \boldsymbol{M}_v\boldsymbol{v}_{\rm r} + \boldsymbol{M}_\omega\boldsymbol{\omega}\right) \tag{7c}$$
$$\dot{\boldsymbol{v}}_{\rm r} = \boldsymbol{v}_{\rm r} \times \boldsymbol{\omega} + \boldsymbol{R}_{\rm IB}^{\mathsf{T}}\boldsymbol{g} + \frac{1}{m}\left(\boldsymbol{F}_0 + \boldsymbol{F}_v\boldsymbol{v}_{\rm r} + \boldsymbol{F}_\omega\boldsymbol{\omega}\right) \tag{7d}$$
$$\dot{\boldsymbol{w}} = \boldsymbol{0} \tag{7e}$$

Assumption 3. *The aircraft's position* $\boldsymbol{q}$*, attitude rotation matrix* $\boldsymbol{R}_{\rm IB}$*, and angular velocity* $\boldsymbol{\omega}$ *are obtained without error.*

Thus, we take $\boldsymbol{y} = (\boldsymbol{q}, \boldsymbol{R}_{\rm IB}, \boldsymbol{\omega}) \in \mathcal{Y} = \mathsf{SE}(3) \times \mathbb{R}^3$ to be the measured part of the state and $\boldsymbol{x} = (\boldsymbol{v}_{\rm r}, \boldsymbol{w}) \in \mathcal{X} = \mathbb{R}^n$ to be the unmeasured part. Here, the dimension of $\mathcal{Y}$ is $p = 9$ ($\mathsf{SE}(3)$ is a 6-dimensional smooth manifold), and the dimension of $\mathcal{X}$ is $n = 6$. The total state space of the system is the $(n+p = 15)$-dimensional manifold $\mathcal{X} \times \mathcal{Y}$. We will use the notation $(\boldsymbol{a}, \boldsymbol{b})$ as shorthand for $[\boldsymbol{a}^\mathsf{T}\ \boldsymbol{b}^\mathsf{T}]^\mathsf{T}$ if $\boldsymbol{a}$ and $\boldsymbol{b}$ are column vectors. More generally, $(\boldsymbol{a}, \boldsymbol{b})$ denotes a point in the product space whose component subspaces are where $\boldsymbol{a}$ and $\boldsymbol{b}$ live, respectively. So, for example, the second element of $\boldsymbol{y}$ lives in $\mathsf{SO}(3)$. With these definitions, the aircraft dynamics (7) are written as

$$\dot{\boldsymbol{x}} = \boldsymbol{f}(\boldsymbol{x}, \boldsymbol{y}, \boldsymbol{u}) \tag{8a}$$

$$\dot{\boldsymbol{y}} = \boldsymbol{h}(\boldsymbol{x}, \boldsymbol{y}, \boldsymbol{u}) \tag{8b}$$

where $\boldsymbol{u}$ is the known "input" to the system. Here, the input vector $\boldsymbol{u}$ is not necessarily flight control inputs; rather it is a collection of known quantities on which a particular transformation group acts. In this case, $\boldsymbol{u}$ is composed of all signals in Eq. (7), other than the system state $(\boldsymbol{x}, \boldsymbol{y})$, that are expressed in either $\mathcal{F}_\mathrm{B}$ or $\mathcal{F}_\mathrm{I}$. That is, $\boldsymbol{u} = (\boldsymbol{g}, \boldsymbol{I}, \boldsymbol{M}_0, \boldsymbol{M}_v, \boldsymbol{M}_\omega, \boldsymbol{F}_0, \boldsymbol{F}_v, \boldsymbol{F}_\omega) \in \mathcal{U}$. The vector field $(\boldsymbol{f}, \boldsymbol{h})$ in Eq. (8) is appropriately constructed from the right-hand side of Eq. (7).

C. Invariance of the Aircraft Dynamics

In order to design a symmetry-preserving observer for the aircraft in wind, we must determine what transformations of the aircraft state and input leave the dynamics (7) unchanged — that is, *invariant*.

1. Mathematical Preliminaries

A Lie group G is said to *act* on a manifold $\mathcal{X}$ via the mapping

$$\boldsymbol{\varphi} : G \times \mathcal{X} \to \mathcal{X},\ (g, \boldsymbol{x}) \mapsto \boldsymbol{\varphi}_g(\boldsymbol{x}) \tag{9}$$

if (i) the identity element e in G induces the identity transformation $\boldsymbol{\varphi}_e(\boldsymbol{x}) = \boldsymbol{x}$ for all $\boldsymbol{x} \in \mathcal{X}$, and (ii) the composition of group actions satisfies $\boldsymbol{\varphi}_g \circ \boldsymbol{\varphi}_h = \boldsymbol{\varphi}_{g*h}$, where "$\circ$" denotes the composition of mappings and "$*$" is group multiplication [31, 32]. Note the inverse transformation $\boldsymbol{\varphi}_g^{-1}$ is given by the action of the inverse group element — i.e., $\boldsymbol{\varphi}_g^{-1} = \boldsymbol{\varphi}_{g^{-1}}$. The collection $\{\boldsymbol{\varphi}_g\}_{g\in G}$ is called a *transformation group*. It is a group in the sense that it satisfies the four group axioms of closure, associativity, existence of an identity, and existence of an inverse.

Transformation groups may be extended to act on the system's inputs as well; that is, G acts on $\mathcal{X} \times \mathcal{U}$. As explained in Refs. [24, 32], a dynamical control system

$$\dot{\boldsymbol{x}} = \boldsymbol{f}(\boldsymbol{x}, \boldsymbol{u}) \tag{10}$$

is called *G-invariant* with respect to the transformation group $\{\boldsymbol{\varphi}_g, \boldsymbol{\psi}_g\}_{g\in G}$ if

$$\boldsymbol{f}(\boldsymbol{\varphi}_g(\boldsymbol{x}), \boldsymbol{\psi}_g(\boldsymbol{u})) = \mathrm{T}_{\boldsymbol{x}}\boldsymbol{\varphi}_g\big(\boldsymbol{f}(\boldsymbol{x}, \boldsymbol{u})\big) \tag{11}$$

where $\mathrm{T}_{\boldsymbol{x}}\boldsymbol{\varphi}_g : \mathsf{T}_{\boldsymbol{x}}\mathcal{X} \to \mathsf{T}_{\boldsymbol{\varphi}_g(\boldsymbol{x})}\mathcal{X}$ denotes the *tangent map* of $\boldsymbol{\varphi}_g$ at $\boldsymbol{x}$ [30, 31]. Note if $\mathcal{X} = \mathbb{R}^n$, then $\mathrm{T}_{\boldsymbol{x}}\boldsymbol{\varphi}_g$ is simply the Jacobian matrix, $\partial\boldsymbol{\varphi}_g(\boldsymbol{x})/\partial\boldsymbol{x}$.

2. $\mathsf{SO}(3)$-*Invariance of the Aircraft Dynamics in Wind*

For the reduced-order observer problem, the aim is to find a transformation group $\{\boldsymbol{\varphi}_g, \boldsymbol{\varrho}_g, \boldsymbol{\psi}_g\}_{g\in G}$ for the system (8), where $\boldsymbol{\varphi}_g$ acts on the unmeasured part of state, $\boldsymbol{\varrho}_g$ acts on the measured part, and $\boldsymbol{\psi}_g$ acts on the input. Recall Lie groups are sets of elements that act on each other through group multiplication, but also topological spaces that correspond (locally) to Euclidean space. As described in Section II.A, the configuration of the rigid-body aircraft is a point on such a manifold — the special Euclidean group $\mathsf{SE}(3)$. Therefore, $\mathsf{SE}(3)$ is a natural choice of Lie group G for which a transformation group is defined (as done by Chen et al. [22], Ahmed and Woolsey [23]). However, since position $\boldsymbol{q}$ does not explicitly appear on the right-hand side of Eq. 7, the translation action of $\mathsf{SE}(3)$ plays no useful role in the observer design. Choosing $G = \mathsf{SO}(3)$ to define the transformation group is sufficient for the construction of an observer.

Furthermore, we recognize the aircraft dynamics are invariant under not just a single $\mathsf{SO}(3)$ transformation group, but rather a family of $\mathsf{SO}(3)$ transformation groups. The two most natural choices from this family are given as follows.

Proposition 1. *The aircraft dynamics* (7) *are* $\mathsf{SO}(3)$-*invariant under the transformation groups*

$$\begin{gathered}
\boldsymbol{\varphi}_g(\boldsymbol{x}) = \begin{pmatrix} \boldsymbol{v}_\mathrm{r} \\ \boldsymbol{R}_g\boldsymbol{w} \end{pmatrix} =: \begin{pmatrix} \boldsymbol{\varphi}_g^{v_\mathrm{r}}(\boldsymbol{x}) \\ \boldsymbol{\varphi}_g^{w}(\boldsymbol{x}) \end{pmatrix} \\
\boldsymbol{\varrho}_g(\boldsymbol{y}) = \begin{pmatrix} \boldsymbol{R}_g\boldsymbol{q} \\ \boldsymbol{R}_g\boldsymbol{R}_\mathrm{IB} \\ \boldsymbol{\omega} \end{pmatrix} =: \begin{pmatrix} \boldsymbol{\varrho}_g^{q}(\boldsymbol{y}) \\ \boldsymbol{\varrho}_g^{R_\mathrm{IB}}(\boldsymbol{y}) \\ \boldsymbol{\varrho}_g^{\omega}(\boldsymbol{y}) \end{pmatrix} \\
\boldsymbol{\psi}_g(\boldsymbol{u}) = \begin{pmatrix} \boldsymbol{R}_g\boldsymbol{g} \\ \boldsymbol{I} \\ \boldsymbol{M}_0 \\ \boldsymbol{M}_v \\ \boldsymbol{M}_\omega \\ \boldsymbol{F}_0 \\ \boldsymbol{F}_v \\ \boldsymbol{F}_\omega \end{pmatrix} =: \begin{pmatrix} \boldsymbol{\psi}_g^{g}(\boldsymbol{u}) \\ \boldsymbol{\psi}_g^{I}(\boldsymbol{u}) \\ \boldsymbol{\psi}_g^{M_0}(\boldsymbol{u}) \\ \boldsymbol{\psi}_g^{M_v}(\boldsymbol{u}) \\ \boldsymbol{\psi}_g^{M_\omega}(\boldsymbol{u}) \\ \boldsymbol{\psi}_g^{F_0}(\boldsymbol{u}) \\ \boldsymbol{\psi}_g^{F_v}(\boldsymbol{u}) \\ \boldsymbol{\psi}_g^{F_\omega}(\boldsymbol{u}) \end{pmatrix}
\end{gathered} \tag{12.I}$$

and

$$\begin{gathered}
\boldsymbol{\varphi}_g(\boldsymbol{x}) = \begin{pmatrix} \boldsymbol{R}_g\boldsymbol{v}_\mathrm{r} \\ \boldsymbol{w} \end{pmatrix} =: \begin{pmatrix} \boldsymbol{\varphi}_g^{v_\mathrm{r}}(\boldsymbol{x}) \\ \boldsymbol{\varphi}_g^{w}(\boldsymbol{x}) \end{pmatrix} \\
\boldsymbol{\varrho}_g(\boldsymbol{y}) = \begin{pmatrix} \boldsymbol{q} \\ \boldsymbol{R}_\mathrm{IB}\boldsymbol{R}_g^\mathsf{T} \\ \boldsymbol{R}_g\boldsymbol{\omega} \end{pmatrix} =: \begin{pmatrix} \boldsymbol{\varrho}_g^{q}(\boldsymbol{y}) \\ \boldsymbol{\varrho}_g^{R_\mathrm{IB}}(\boldsymbol{y}) \\ \boldsymbol{\varrho}_g^{\omega}(\boldsymbol{y}) \end{pmatrix} \\
\boldsymbol{\psi}_g(\boldsymbol{u}) = \begin{pmatrix} \boldsymbol{g} \\ \boldsymbol{R}_g\boldsymbol{I}\boldsymbol{R}_g^\mathsf{T} \\ \boldsymbol{R}_g\boldsymbol{M}_0 \\ \boldsymbol{R}_g\boldsymbol{M}_v\boldsymbol{R}_g^\mathsf{T} \\ \boldsymbol{R}_g\boldsymbol{M}_\omega\boldsymbol{R}_g^\mathsf{T} \\ \boldsymbol{R}_g\boldsymbol{F}_0 \\ \boldsymbol{R}_g\boldsymbol{F}_v\boldsymbol{R}_g^\mathsf{T} \\ \boldsymbol{R}_g\boldsymbol{F}_\omega\boldsymbol{R}_g^\mathsf{T} \end{pmatrix} =: \begin{pmatrix} \boldsymbol{\psi}_g^{g}(\boldsymbol{u}) \\ \boldsymbol{\psi}_g^{I}(\boldsymbol{u}) \\ \boldsymbol{\psi}_g^{M_0}(\boldsymbol{u}) \\ \boldsymbol{\psi}_g^{M_v}(\boldsymbol{u}) \\ \boldsymbol{\psi}_g^{M_\omega}(\boldsymbol{u}) \\ \boldsymbol{\psi}_g^{F_0}(\boldsymbol{u}) \\ \boldsymbol{\psi}_g^{F_v}(\boldsymbol{u}) \\ \boldsymbol{\psi}_g^{F_\omega}(\boldsymbol{u}) \end{pmatrix}
\end{gathered} \tag{12.B}$$

where $g = \boldsymbol{R}_g \in \mathsf{SO}(3)$.

The proof of Proposition 1 is given in Appendix A.

Both transformation groups characterize the rotational symmetry of the aircraft dynamics. Since the transformation group defined by Eq. (12.I) consists of rotations of inertial frame quantities, we call it the *inertial transformation group*. This transformation group reflects the fact that the orientation of the inertial frame is arbitrary. Conversely, Eq. (12.B) consists of rotations of body frame quantities and thus is called the *body transformation group*. Its definition recognizes that the orientation of the body frame is also arbitrary as long as parameters (e.g., aerodynamic force and moment parameters) are appropriately expressed in the rotated coordinate frame. When appropriate, we will append equation numbers with "I" or "B" when they apply to transformation groups (12.I) or (12.B), respectively. These labels will resolve the ambiguity from different definitions of $\boldsymbol{\varphi}$, $\boldsymbol{\varrho}$, and $\boldsymbol{\psi}$.

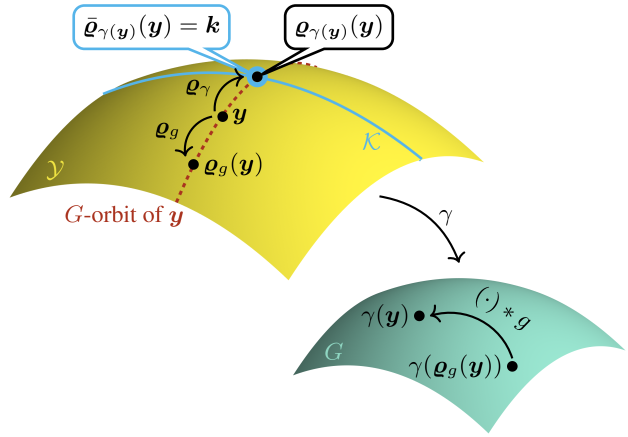

Fig. 1 Equivariance of the moving frame γ and its construction via the cross-section $\mathcal{K}$.

III. Symmetry-Preserving Reduced-Order Wind Observers

Now that we have established how the dynamics (8) are $\mathsf{SO}(3)$-invariant, the theory developed by the authors in Ref. [29] can be used to obtain reduced-order observers that preserve the symmetries associated with transformation groups (12.I) and (12.B).

A. The Moving Frame

To preserve symmetries in the observer dynamics, we make use of a *moving frame* [32, Ch. 8], which can be used to find invariant functions of the system's state. The moving frame is intimately tied to how sets of transformed points $\{\boldsymbol{\varrho}_g(\boldsymbol{y}) \in \mathcal{Y} \mid g \in G\}$, called *$G$-orbits*, relate to the composition of Lie group actions. For our problem, we only need to consider the transformation on the measured part of the state, $\boldsymbol{\varrho}_g(\boldsymbol{y})$. Therefore, it is sufficient to consider a *moving frame* to be a mapping $\gamma : \mathcal{Y} \to G$ that has the following *equivariance* property.

$$\gamma(\boldsymbol{\varrho}_g(\boldsymbol{y})) * g = \gamma(\boldsymbol{y}) \tag{13}$$

Geometrically, the moving frame may be viewed as the map from the state space to the Lie group element that transforms points to a chosen *cross-section* — a submanifold $\mathcal{K} \subset \mathcal{Y}$ that transversely intersects G-orbits on $\mathcal{Y}$. This interpretation provides a method for constructing a moving frame [24, 32], which we summarize as follows.

Suppose the r-dimensional Lie group G *acts freely* on the p-dimensional manifold $\mathcal{Y}$; that is, $\boldsymbol{\varrho}_g(\boldsymbol{y}) = \boldsymbol{y}$ implies g is the identity element, e. For fixed $\boldsymbol{y} \in \mathcal{Y}$, the map $\boldsymbol{\varrho}_{(\cdot)}(\boldsymbol{y}) : G \to \mathcal{Y}$ is non-surjective, only mapping to points on the G-orbit of $\boldsymbol{y}$ (the red dashed line in Figure 1). However, one can identify the r-dimensional part $\bar{\boldsymbol{\varrho}}_{(\cdot)}(\boldsymbol{y})$ of the map $\boldsymbol{\varrho}_{(\cdot)}(\boldsymbol{y})$ that is invertible (i.e., bijective) on $\bar{\mathcal{Y}} \subset \mathcal{Y}$. As depicted in Figure 1, one can select a constant $\boldsymbol{k}$ in the image of $\bar{\boldsymbol{\varrho}}$ that defines the unique point at which the G-orbit of a generic point $\boldsymbol{y}$ intersects the $(p-r)$-dimensional cross-section

$$\mathcal{K} = \{\boldsymbol{y} \in \mathcal{Y} \mid \bar{\boldsymbol{\varrho}}_e(\boldsymbol{y}) = \boldsymbol{k}\}$$

In other words, the moving frame is obtained by solving the *normalization equation*

$$\bar{\boldsymbol{\varrho}}_h(\boldsymbol{y}) = \boldsymbol{k} \tag{14}$$

for $h \in G$. The solution $h = \gamma(\boldsymbol{y})$ defines the moving frame $\gamma : \mathcal{Y} \to G$.

Since the attitude state space of the system is $G = \mathsf{SO}(3)$ itself, the *moving frame* $\gamma : \mathcal{Y} \to G$ is naturally defined by the element of $\mathsf{SO}(3)$ whose action on the rotational configuration yields the identity element, $e = \mathbb{I}$. Therefore, $\bar{\mathcal{Y}} = \mathsf{SO}(3)$ and the normalization equations read

$$\boldsymbol{R}_h \boldsymbol{R}_{\mathrm{IB}} = \mathbb{I} \tag{15.I}$$

$$\boldsymbol{R}_{\mathrm{IB}} \boldsymbol{R}_h^{\mathsf{T}} = \mathbb{I} \tag{15.B}$$

which imply

$$h = \gamma(\boldsymbol{y}) = \boldsymbol{R}_{\mathrm{IB}}^{\mathsf{T}} \tag{16.I}$$

$$h = \gamma(\boldsymbol{y}) = \boldsymbol{R}_{\mathrm{IB}} \tag{16.B}$$

are the group elements that define moving frames with the equivariance property (13). The moving frame will be used to construct an invariant mapping from the measured states to estimates of the unmeasured states, which is then used to define the form of the symmetry-preserving reduced-order observer (Section III.B) and obtain sufficient conditions for its stability (Section III.C).

B. Invariant Pre-Observer

With moving frames identified, we can construct symmetry-preserving reduced-order observers, defined as follows.

Definition 1 ([29]). *The dynamical system*

$$\dot{\boldsymbol{z}} = \boldsymbol{\alpha}(\boldsymbol{z}, \boldsymbol{y}, \boldsymbol{u}) \tag{17}$$

with output

$$\hat{\boldsymbol{x}} = \boldsymbol{z} + \boldsymbol{\beta}(\boldsymbol{y}) \tag{18}$$

for some smooth map $\boldsymbol{\beta} : \mathcal{Y} \to \mathcal{X}$ is a <u>*G-invariant reduced-order pre-observer*</u> *if the system*

$$\dot{\hat{\boldsymbol{x}}} = \boldsymbol{\alpha}(\hat{\boldsymbol{x}} - \boldsymbol{\beta}(\boldsymbol{y}), \boldsymbol{y}, \boldsymbol{u}) + \mathrm{T}_{\boldsymbol{y}}\boldsymbol{\beta}\big(\boldsymbol{h}(\boldsymbol{x}, \boldsymbol{y}, \boldsymbol{u})\big) \tag{19}$$

is G-invariant and the manifold

$$\mathcal{Z} = \{(\boldsymbol{z}, \boldsymbol{x}, \boldsymbol{y}) \in \mathcal{X} \times \mathcal{X} \times \mathcal{Y} \mid \boldsymbol{z} = \boldsymbol{x} - \boldsymbol{\beta}(\boldsymbol{y})\} \tag{20}$$

is positively invariant. A G-invariant pre-observer is a <u>*G-invariant observer*</u> *if $\mathcal{Z}$ is asymptotically attractive.*

The key to constructing the pre-observer (17) is the choice of $\boldsymbol{\beta}$, which we call the *observer map*. From Lemma 1 in Ref. [29], let

$$\boldsymbol{\beta}(\boldsymbol{y}) = \boldsymbol{\varphi}_{\gamma(\boldsymbol{y})^{-1}}\Big(\boldsymbol{\ell}\big(\boldsymbol{\varrho}_{\gamma(\boldsymbol{y})}(\boldsymbol{y})\big)\Big) \tag{21}$$

where $\boldsymbol{\ell} : \mathcal{Y} \to \mathcal{X}$ is a smooth map, called the *gain map*. As illustrated in Figure 2, this choice of $\boldsymbol{\beta}$ is special in that it commutes with the transformation group. That is,

$$\boldsymbol{\varphi}_g(\boldsymbol{\beta}(\boldsymbol{y})) = \boldsymbol{\beta}(\boldsymbol{\varrho}_g(\boldsymbol{y})) \tag{22}$$

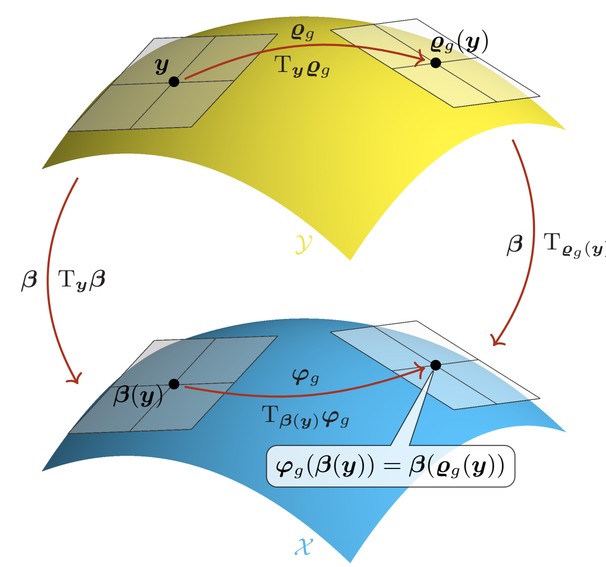

Fig. 2 Commutative relationship between $\boldsymbol{\beta}$ and the transformation group.

Inspecting the choice of $\boldsymbol{\beta}$ in Eq. (21), we notice that $\boldsymbol{\varrho}^{R_{\mathrm{IB}}}_{\gamma(\boldsymbol{y})}(\boldsymbol{y}) = \mathbb{I}$. Therefore, we need only consider $\boldsymbol{\ell} : \mathcal{Y} \setminus \mathsf{SO}(3) \to \mathcal{X}$. Let

$$\boldsymbol{\ell}(\boldsymbol{y}) = \underbrace{\begin{bmatrix} \boldsymbol{L}^q_{v_\mathrm{r}} & \boldsymbol{L}^\omega_{v_\mathrm{r}} \\ \boldsymbol{L}^q_w & \boldsymbol{L}^\omega_w \end{bmatrix}}_{\boldsymbol{L}} \begin{bmatrix} \boldsymbol{q} \\ \boldsymbol{\omega} \end{bmatrix} \tag{23}$$

where $\boldsymbol{L}$ is the *observer gain matrix* which we allow to vary with time. With this choice of the gain map $\boldsymbol{\ell}$, the observer map $\boldsymbol{\beta}$ in Eq. (21) becomes

$$\boldsymbol{\beta}(\boldsymbol{y}) = \begin{bmatrix} \boldsymbol{L}^q_{v_\mathrm{r}} \boldsymbol{R}_{\mathrm{IB}}^\mathsf{T} \boldsymbol{q} + \boldsymbol{L}^\omega_{v_\mathrm{r}} \boldsymbol{\omega} \\ \boldsymbol{R}_{\mathrm{IB}} \boldsymbol{L}^q_w \boldsymbol{R}_{\mathrm{IB}}^\mathsf{T} \boldsymbol{q} + \boldsymbol{R}_{\mathrm{IB}} \boldsymbol{L}^\omega_w \boldsymbol{\omega} \end{bmatrix} \tag{24.I}$$

$$\boldsymbol{\beta}(\boldsymbol{y}) = \begin{bmatrix} \boldsymbol{R}_{\mathrm{IB}}^\mathsf{T} \boldsymbol{L}^q_{v_\mathrm{r}} \boldsymbol{q} + \boldsymbol{R}_{\mathrm{IB}}^\mathsf{T} \boldsymbol{L}^\omega_{v_\mathrm{r}} \boldsymbol{R}_{\mathrm{IB}} \boldsymbol{\omega} \\ \boldsymbol{L}^q_w \boldsymbol{q} + \boldsymbol{L}^\omega_w \boldsymbol{R}_{\mathrm{IB}} \boldsymbol{\omega} \end{bmatrix} \tag{24.B}$$

Next, we use Theorem 1 in Ref. [29] to obtain an expression for the observer dynamics vector field $\boldsymbol{\alpha}$ that yields a G-invariant pre-observer.

Theorem 1 ([29])**.** *Suppose $\boldsymbol{\beta}$ is given by Eq.* (21) *and that $\boldsymbol{\varphi}_g(\boldsymbol{x})$ is linear in $\boldsymbol{x}$. Let the vector field $\boldsymbol{\alpha}(\cdot, \boldsymbol{y}, \boldsymbol{u}) : \mathcal{X} \to \mathsf{T}\mathcal{X}$ be defined by*

$$\boldsymbol{\alpha}(\boldsymbol{z}, \boldsymbol{y}, \boldsymbol{u}) = \boldsymbol{f}(\boldsymbol{z} + \boldsymbol{\beta}(\boldsymbol{y}), \boldsymbol{y}, \boldsymbol{u}) - \mathrm{T}_{\boldsymbol{y}}\boldsymbol{\beta}\big(\boldsymbol{h}(\boldsymbol{z} + \boldsymbol{\beta}(\boldsymbol{y}), \boldsymbol{y}, \boldsymbol{u})\big) \tag{25}$$

Then, the dynamical system (17) *with output* (18) *is a G-invariant, reduced-order pre-observer.*

Applying this theorem, we write the components of $\boldsymbol{\alpha}$ as

$$\begin{aligned} \boldsymbol{\alpha}_{v_\mathrm{r}}(\boldsymbol{z}, \boldsymbol{y}, \boldsymbol{u}) &= \hat{\boldsymbol{v}}_\mathrm{r} \times \boldsymbol{\omega} + \boldsymbol{R}_{\mathrm{IB}}^\mathsf{T} \boldsymbol{g} + \frac{1}{m}\left(\boldsymbol{F}_0 + \boldsymbol{F}_v \hat{\boldsymbol{v}}_\mathrm{r} + \boldsymbol{F}_\omega \boldsymbol{\omega}\right) \\ &- \boldsymbol{L}^q_{v_\mathrm{r}} \boldsymbol{R}_{\mathrm{IB}}^\mathsf{T}\left(\boldsymbol{R}_{\mathrm{IB}} \hat{\boldsymbol{v}}_\mathrm{r} + \hat{\boldsymbol{w}}\right) - \boldsymbol{L}^\omega_{v_\mathrm{r}} \boldsymbol{I}^{-1}\big(\boldsymbol{I}\boldsymbol{\omega} \times \boldsymbol{\omega} + \boldsymbol{M}_0 + \boldsymbol{M}_v \hat{\boldsymbol{v}}_\mathrm{r} \\ &+ \boldsymbol{M}_\omega \boldsymbol{\omega}\big) + \boldsymbol{L}^q_{v_\mathrm{r}} \boldsymbol{S}(\boldsymbol{\omega}) \boldsymbol{R}_{\mathrm{IB}}^\mathsf{T} \boldsymbol{q} - \dot{\boldsymbol{L}}^q_{v_\mathrm{r}} \boldsymbol{R}_{\mathrm{IB}}^\mathsf{T} \boldsymbol{q} - \dot{\boldsymbol{L}}^\omega_{v_\mathrm{r}} \boldsymbol{\omega} \end{aligned} \tag{26.I}$$

$$\begin{aligned} \boldsymbol{\alpha}_{v_\mathrm{r}}(\boldsymbol{z}, \boldsymbol{y}, \boldsymbol{u}) &= \hat{\boldsymbol{v}}_\mathrm{r} \times \boldsymbol{\omega} + \boldsymbol{R}_{\mathrm{IB}}^\mathsf{T} \boldsymbol{g} + \frac{1}{m}\left(\boldsymbol{F}_0 + \boldsymbol{F}_v \hat{\boldsymbol{v}}_\mathrm{r} + \boldsymbol{F}_\omega \boldsymbol{\omega}\right) \\ &- \boldsymbol{R}_{\mathrm{IB}}^\mathsf{T} \boldsymbol{L}^q_{v_\mathrm{r}}\left(\boldsymbol{R}_{\mathrm{IB}} \hat{\boldsymbol{v}}_\mathrm{r} + \hat{\boldsymbol{w}}\right) - \boldsymbol{R}_{\mathrm{IB}}^\mathsf{T} \boldsymbol{L}^\omega_{v_\mathrm{r}} \boldsymbol{R}_{\mathrm{IB}} \boldsymbol{I}^{-1}\big(\boldsymbol{I}\boldsymbol{\omega} \times \boldsymbol{\omega} + \boldsymbol{M}_0 \\ &+ \boldsymbol{M}_v \hat{\boldsymbol{v}}_\mathrm{r} + \boldsymbol{M}_\omega \boldsymbol{\omega}\big) + \boldsymbol{S}(\boldsymbol{\omega}) \boldsymbol{R}_{\mathrm{IB}}^\mathsf{T} \boldsymbol{L}^q_{v_\mathrm{r}} \boldsymbol{q} + \boldsymbol{S}(\boldsymbol{\omega}) \boldsymbol{R}_{\mathrm{IB}}^\mathsf{T} \boldsymbol{L}^\omega_{v_\mathrm{r}} \boldsymbol{R}_{\mathrm{IB}} \boldsymbol{\omega} \\ &- \boldsymbol{R}_{\mathrm{IB}}^\mathsf{T} \dot{\boldsymbol{L}}^q_{v_\mathrm{r}} \boldsymbol{q} - \boldsymbol{R}_{\mathrm{IB}}^\mathsf{T} \dot{\boldsymbol{L}}^\omega_{v_\mathrm{r}} \boldsymbol{R}_{\mathrm{IB}} \boldsymbol{\omega} \end{aligned} \tag{26.B}$$

and

$$\begin{aligned} \boldsymbol{\alpha}_w(\boldsymbol{z}, \boldsymbol{y}, \boldsymbol{u}) &= -\boldsymbol{R}_{\mathrm{IB}} \boldsymbol{L}^q_w \boldsymbol{R}_{\mathrm{IB}}^\mathsf{T}\left(\boldsymbol{R}_{\mathrm{IB}} \hat{\boldsymbol{v}}_\mathrm{r} + \hat{\boldsymbol{w}}\right) \\ &- \boldsymbol{R}_{\mathrm{IB}} \boldsymbol{L}^\omega_w \boldsymbol{I}^{-1}\left(\boldsymbol{I}\boldsymbol{\omega} \times \boldsymbol{\omega} + \boldsymbol{M}_0 + \boldsymbol{M}_v \hat{\boldsymbol{v}}_\mathrm{r} + \boldsymbol{M}_\omega \boldsymbol{\omega}\right) \\ &- \boldsymbol{R}_{\mathrm{IB}} \boldsymbol{S}(\boldsymbol{\omega}) \boldsymbol{L}^\omega_w \boldsymbol{\omega} - \boldsymbol{R}_{\mathrm{IB}}\left(\boldsymbol{S}(\boldsymbol{\omega}) \boldsymbol{L}^q_w - \boldsymbol{L}^q_w \boldsymbol{S}(\boldsymbol{\omega})\right) \boldsymbol{R}_{\mathrm{IB}}^\mathsf{T} \boldsymbol{q} \\ &- \boldsymbol{R}_{\mathrm{IB}} \dot{\boldsymbol{L}}^q_w \boldsymbol{R}_{\mathrm{IB}}^\mathsf{T} \boldsymbol{q} - \boldsymbol{R}_{\mathrm{IB}} \dot{\boldsymbol{L}}^\omega_w \boldsymbol{\omega} \end{aligned} \tag{27.I}$$

$$\begin{aligned} \boldsymbol{\alpha}_w(\boldsymbol{z}, \boldsymbol{y}, \boldsymbol{u}) &= -\boldsymbol{L}^q_w\left(\boldsymbol{R}_{\mathrm{IB}} \hat{\boldsymbol{v}}_\mathrm{r} + \hat{\boldsymbol{w}}\right) - \boldsymbol{L}^\omega_w \boldsymbol{R}_{\mathrm{IB}} \boldsymbol{I}^{-1}\big(\boldsymbol{I}\boldsymbol{\omega} \times \boldsymbol{\omega} \\ &+ \boldsymbol{M}_0 + \boldsymbol{M}_v \hat{\boldsymbol{v}}_\mathrm{r} + \boldsymbol{M}_\omega \boldsymbol{\omega}\big) - \dot{\boldsymbol{L}}^q_w \boldsymbol{q} - \dot{\boldsymbol{L}}^\omega_w \boldsymbol{R}_{\mathrm{IB}} \boldsymbol{\omega} \end{aligned} \tag{27.B}$$

for transformation groups (12.I) and (12.B), respectively, where

$$\begin{aligned} \hat{\boldsymbol{v}}_\mathrm{r} &= \boldsymbol{z}_{v_\mathrm{r}} + \boldsymbol{L}^q_{v_\mathrm{r}} \boldsymbol{R}_{\mathrm{IB}}^\mathsf{T} \boldsymbol{q} + \boldsymbol{L}^\omega_{v_\mathrm{r}} \boldsymbol{\omega} \\ \hat{\boldsymbol{w}} &= \boldsymbol{z}_w + \boldsymbol{R}_{\mathrm{IB}} \boldsymbol{L}^q_w \boldsymbol{R}_{\mathrm{IB}}^\mathsf{T} \boldsymbol{q} + \boldsymbol{R}_{\mathrm{IB}} \boldsymbol{L}^\omega_w \boldsymbol{\omega} \end{aligned} \tag{28.I}$$

$$\begin{aligned} \hat{\boldsymbol{v}}_\mathrm{r} &= \boldsymbol{z}_{v_\mathrm{r}} + \boldsymbol{R}_{\mathrm{IB}}^\mathsf{T} \boldsymbol{L}^q_{v_\mathrm{r}} \boldsymbol{q} + \boldsymbol{R}_{\mathrm{IB}}^\mathsf{T} \boldsymbol{L}^\omega_{v_\mathrm{r}} \boldsymbol{R}_{\mathrm{IB}} \boldsymbol{\omega} \\ \hat{\boldsymbol{w}} &= \boldsymbol{z}_w + \boldsymbol{L}^q_w \boldsymbol{q} + \boldsymbol{L}^\omega_w \boldsymbol{R}_{\mathrm{IB}} \boldsymbol{\omega} \end{aligned} \tag{28.B}$$

are the corresponding state estimates.

C. Invariant Observer

We now aim to choose the gain matrix $\boldsymbol{L}$ such that the pre-observer given by Eqs. (17) and (18) is a G-invariant reduced-order *observer*. That is, we seek sufficient conditions for which the zero-error manifold $\mathcal{Z}$ is asymptotically attractive. Consider the *invariant error coordinates*

$$\boldsymbol{\eta}(\boldsymbol{z}, \boldsymbol{x}, \boldsymbol{y}) = \boldsymbol{\varphi}_{\gamma(\boldsymbol{y})}(\boldsymbol{z}) + \boldsymbol{\ell}(\boldsymbol{\varrho}_{\gamma(\boldsymbol{y})}(\boldsymbol{y})) - \boldsymbol{\varphi}_{\gamma(\boldsymbol{y})}(\boldsymbol{x}) \tag{29}$$

They are invariant in the sense that $\boldsymbol{\eta} : \mathcal{X} \times \mathcal{X} \times \mathcal{Y} \to \mathcal{X}$ is an invariant map. They are valid error coordinates because $\boldsymbol{\eta} = \boldsymbol{0}$ if and only if $(\boldsymbol{z}, \boldsymbol{x}, \boldsymbol{y}) \in \mathcal{Z}$, the zero-error manifold prescribed in Eq. (20).

Consider the following definitions. Let $\boldsymbol{\lambda} : \mathcal{Y} \to \mathcal{X}$ be the map

$$\boldsymbol{\lambda}(\boldsymbol{y}; \boldsymbol{\eta}) = \boldsymbol{\varphi}_{\gamma(\boldsymbol{y})}(\boldsymbol{\eta})$$

where $\boldsymbol{\eta} \in \mathcal{X}$ is held constant. Using the moving frame (16), let

$$\boldsymbol{X} = \boldsymbol{\varphi}_{\gamma(\boldsymbol{y})}(\boldsymbol{x}), \quad \boldsymbol{Y} = \boldsymbol{\varrho}_{\gamma(\boldsymbol{y})}(\boldsymbol{y}), \quad \boldsymbol{U} = \boldsymbol{\psi}_{\gamma(\boldsymbol{y})}(\boldsymbol{u}) \tag{30}$$

which, by construction, are invariant functions of the system state and input [32, Ch. 8]. Then, Theorem 2 of Ref. [29] gives an invariant error system whose stability is a sufficient condition for the pre-observer given by Eqs. (17) and (18) to be a G-invariant reduced-order observer; that is, $\hat{\boldsymbol{x}} \to \boldsymbol{x}$ as $t \to \infty$.

Theorem 2 ([29])**.** *Suppose the assumptions of Theorem 1 hold. The G-invariant pre-observer* (17) *is a G-invariant observer if the origin $\boldsymbol{\eta} = \mathbf{0}$ of the* invariant error system

$$\begin{aligned}\dot{\boldsymbol{\eta}} = \boldsymbol{f}(\boldsymbol{X}+\boldsymbol{\eta},\boldsymbol{Y},\boldsymbol{U}) - \boldsymbol{f}(\boldsymbol{X},\boldsymbol{Y},\boldsymbol{U}) \\ - \mathrm{T}_{\boldsymbol{Y}}\boldsymbol{\beta}\big(\boldsymbol{h}(\boldsymbol{X}+\boldsymbol{\eta},\boldsymbol{Y},\boldsymbol{U}) - \boldsymbol{h}(\boldsymbol{X},\boldsymbol{Y},\boldsymbol{U})\big) \\ + \mathrm{T}_{(\boldsymbol{Y};\boldsymbol{\eta})}\boldsymbol{\lambda}\big(\boldsymbol{h}(\boldsymbol{X},\boldsymbol{Y},\boldsymbol{U})\big)\end{aligned} \quad (31)$$

is asymptotically stable, uniformly in $\boldsymbol{X}$, $\boldsymbol{Y}$, and $\boldsymbol{U}$.

To apply Theorem 2, we expand and simplify Eq. (31) to obtain the invariant error dynamics

$$\begin{aligned}\dot{\boldsymbol{\eta}}_{v_\mathrm{r}} &= -\boldsymbol{S}(\boldsymbol{\omega})\boldsymbol{\eta}_{v_\mathrm{r}} + \tfrac{1}{m}\boldsymbol{F}_v\boldsymbol{\eta}_{v_\mathrm{r}} - \boldsymbol{L}^q_{v_\mathrm{r}}(\boldsymbol{\eta}_{v_\mathrm{r}} + \boldsymbol{\eta}_w) - \boldsymbol{L}^\omega_{v_\mathrm{r}}\boldsymbol{I}^{-1}\boldsymbol{M}_v\boldsymbol{\eta}_{v_\mathrm{r}} \\ \dot{\boldsymbol{\eta}}_w &= -\boldsymbol{L}^q_w(\boldsymbol{\eta}_{v_\mathrm{r}} + \boldsymbol{\eta}_w) - \boldsymbol{L}^\omega_w\boldsymbol{I}^{-1}\boldsymbol{M}_v\boldsymbol{\eta}_{v_\mathrm{r}}\end{aligned} \quad (32.\mathrm{I})$$

$$\begin{aligned}\dot{\boldsymbol{\eta}}_{v_\mathrm{r}} &= \tfrac{1}{m}\boldsymbol{R}_\mathrm{IB}\boldsymbol{F}_v\boldsymbol{R}_\mathrm{IB}^\mathsf{T}\boldsymbol{\eta}_{v_\mathrm{r}} - \boldsymbol{L}^q_{v_\mathrm{r}}(\boldsymbol{\eta}_{v_\mathrm{r}} + \boldsymbol{\eta}_w) - \boldsymbol{L}^\omega_{v_\mathrm{r}}\boldsymbol{R}_\mathrm{IB}\boldsymbol{I}^{-1}\boldsymbol{M}_v\boldsymbol{R}_\mathrm{IB}^\mathsf{T}\boldsymbol{\eta}_{v_\mathrm{r}} \\ \dot{\boldsymbol{\eta}}_w &= -\boldsymbol{L}^q_w(\boldsymbol{\eta}_{v_\mathrm{r}} + \boldsymbol{\eta}_w) - \boldsymbol{L}^\omega_w\boldsymbol{R}_\mathrm{IB}\boldsymbol{I}^{-1}\boldsymbol{M}_v\boldsymbol{R}_\mathrm{IB}^\mathsf{T}\boldsymbol{\eta}_{v_\mathrm{r}}\end{aligned} \quad (32.\mathrm{B})$$

Notice that for the body transformation group, the transformed input signal appears as $\boldsymbol{R}_\mathrm{IB}\boldsymbol{F}_v\boldsymbol{R}_\mathrm{IB}^\mathsf{T} = \boldsymbol{U}_{F_v}$ and $\boldsymbol{R}_\mathrm{IB}\boldsymbol{I}^{-1}\boldsymbol{M}_v\boldsymbol{R}_\mathrm{IB}^\mathsf{T} = \boldsymbol{U}_I\boldsymbol{U}_{M_v}$.

Remark 1. *The error system* (32) *depends only on the invariant error $\boldsymbol{\eta}$ and the invariants $\boldsymbol{Y}$ and $\boldsymbol{U}$, which together with $\boldsymbol{X}$ form a set of $n+p-r$ functionally independent invariants $\boldsymbol{I}(\boldsymbol{x},\boldsymbol{y},\boldsymbol{u})$ [32, Ch. 8]. This observation is consistent with the full-order case considered by Bonnabel et al. [24, Theorem 3].*

We now aim to choose the dynamics of the matrix $\boldsymbol{L}$ to render $\boldsymbol{\eta} = \mathbf{0}$ asymptotically stable. Equation (32) can be viewed as a linear, time-varying (LTV) system since $\boldsymbol{Y}$ and $\boldsymbol{U}$ are known signals. Therefore, the stabilization of the invariant error system is reduced to LTV observer design for the fictitious system

$$\begin{aligned}\dot{\boldsymbol{\xi}} &= \boldsymbol{A}(t)\boldsymbol{\xi} \\ \boldsymbol{\zeta} &= \boldsymbol{C}(t)\boldsymbol{\xi}\end{aligned} \quad (33)$$

where

$$\begin{aligned}\boldsymbol{A}(t) &= \begin{bmatrix} -\boldsymbol{S}(\boldsymbol{\omega}(t)) + \boldsymbol{F}_v(t)/m & \mathbf{0} \\ \mathbf{0} & -\boldsymbol{S}(\boldsymbol{\omega}(t))\end{bmatrix}, \\ \boldsymbol{C}(t) &= \begin{bmatrix} \mathbb{I} & \mathbb{I} \\ \boldsymbol{I}^{-1}\boldsymbol{M}_v(t) & \mathbf{0}\end{bmatrix}\end{aligned} \quad (34.\mathrm{I})$$

$$\begin{aligned}\boldsymbol{A}(t) &= \begin{bmatrix} \boldsymbol{R}_\mathrm{IB}(t)\boldsymbol{F}_v(t)\boldsymbol{R}_\mathrm{IB}^\mathsf{T}(t)/m & \mathbf{0} \\ \mathbf{0} & \mathbf{0}\end{bmatrix}, \\ \boldsymbol{C}(t) &= \begin{bmatrix} \mathbb{I} & \mathbb{I} \\ \boldsymbol{R}_\mathrm{IB}(t)\boldsymbol{I}^{-1}\boldsymbol{M}_v(t)\boldsymbol{R}_\mathrm{IB}^\mathsf{T}(t) & \mathbf{0}\end{bmatrix}\end{aligned} \quad (34.\mathrm{B})$$

Using $\boldsymbol{L}(t)$ as the linear observer gain matrix for the system (33), the closed-loop error dynamics

$$\dot{\boldsymbol{\eta}} = (\boldsymbol{A}(t) - \boldsymbol{L}(t)\boldsymbol{C}(t))\,\boldsymbol{\eta} \quad (35)$$

are exactly the invariant error system (32). Therefore, one must simply choose positive definite matrices $\boldsymbol{Q}$ and $\boldsymbol{R}$ (which may be time-varying), propagate the differential Riccati equation

$$\begin{aligned}\dot{\boldsymbol{P}}(t) = \boldsymbol{A}(t)\boldsymbol{P}(t) + \boldsymbol{P}(t)\boldsymbol{A}^\mathsf{T}(t) \\ - \boldsymbol{P}(t)\boldsymbol{C}^\mathsf{T}(t)\boldsymbol{R}^{-1}(t)\boldsymbol{C}(t)\boldsymbol{P}(t) + \boldsymbol{Q}(t)\end{aligned} \quad (36)$$

and let

$$\boldsymbol{L}(t) = \boldsymbol{P}(t)\boldsymbol{C}^\mathsf{T}(t)\boldsymbol{R}^{-1}(t) \quad (37)$$

The preceding discussion proves the main result of this paper:

Theorem 3. *If the pair $(\boldsymbol{A}(t), \boldsymbol{C}(t))$ is observable, then the $\mathsf{SO}(3)$-invariant pre-observer* (17) *with $\boldsymbol{\alpha}$ given by Eq.* (25) *and $\boldsymbol{L}(t)$ satisfying Eq.* (37) *is an exponentially stable $\mathsf{SO}(3)$-invariant observer for the aircraft in wind given by Eq.* (7)*.*

The observability of $(\boldsymbol{A}(t), \boldsymbol{C}(t))$ is not overly restrictive. Most nonlinear aerodynamic models for both fixed-wing and multirotor aircraft satisfy this observability requirement. For example, constructing $\boldsymbol{F}_v$ and $\boldsymbol{M}_v$ from the large-domain fixed-wing and multirotor models given in [33] and [34], respectively, both yield observability.

IV. Practical Implementation

Since most large-domain aerodynamic models do not satisfy Assumption 2, the time-varying parameters $\boldsymbol{F}_{(\cdot)}$, $\boldsymbol{M}_{(\cdot)}$ must be constructed using the current estimate of the air-relative velocity $\boldsymbol{v}_\mathrm{r}$ — akin to linearizing about the best estimate in an extended Kalman filter. Using the force model as an example, we often consider smooth, nonlinear, quasi-steady aerodynamic models $\boldsymbol{F}(\boldsymbol{v}_\mathrm{r}, \boldsymbol{\omega}, \boldsymbol{\delta})$, where $\boldsymbol{\delta}$ is the vector of flight control inputs (e.g., throttle setting and control surface deflections). Performing a Taylor series expansion about $\hat{\boldsymbol{v}}_\mathrm{r}$, we have

$$\boldsymbol{F}(\boldsymbol{v}_\mathrm{r}, \boldsymbol{\omega}, \boldsymbol{\delta}) = \boldsymbol{F}(\hat{\boldsymbol{v}}_\mathrm{r}, \boldsymbol{\omega}, \boldsymbol{\delta}) + \underbrace{\left.\frac{\partial \boldsymbol{F}}{\partial \boldsymbol{v}_\mathrm{r}}\right|_{\boldsymbol{v}_\mathrm{r} = \hat{\boldsymbol{v}}_\mathrm{r}}}_{\boldsymbol{F}_v(\hat{\boldsymbol{v}}_\mathrm{r}, \boldsymbol{\omega}, \boldsymbol{\delta})}(\boldsymbol{v}_\mathrm{r} - \hat{\boldsymbol{v}}_\mathrm{r}) + \text{H.O.T.} \quad (38)$$

Noting that any smooth function $\boldsymbol{f}(\boldsymbol{x})$ may be written as $\boldsymbol{A}(\boldsymbol{x})\boldsymbol{x} + \boldsymbol{b}(\boldsymbol{x})$, one may write

$$\boldsymbol{F}(\hat{\boldsymbol{v}}_\mathrm{r}, \boldsymbol{\omega}, \boldsymbol{\delta}) = \boldsymbol{F}_\omega(\hat{\boldsymbol{v}}_\mathrm{r}, \boldsymbol{\omega}, \boldsymbol{\delta})\boldsymbol{\omega} + \bar{\boldsymbol{F}}_0(\hat{\boldsymbol{v}}_\mathrm{r}, \boldsymbol{\omega}, \boldsymbol{\delta}) \quad (39)$$

Then, letting $\boldsymbol{F}_0(\hat{\boldsymbol{v}}_\mathrm{r}, \boldsymbol{\omega}, \boldsymbol{\delta}) = \bar{\boldsymbol{F}}_0(\hat{\boldsymbol{v}}_\mathrm{r}, \boldsymbol{\omega}, \boldsymbol{\delta}) - \boldsymbol{F}_v(\hat{\boldsymbol{v}}_\mathrm{r}, \boldsymbol{\omega}, \boldsymbol{\delta})\hat{\boldsymbol{v}}_\mathrm{r}$ yields

$$\begin{aligned}\boldsymbol{F}(\boldsymbol{v}_\mathrm{r}, \boldsymbol{\omega}, \boldsymbol{\delta}) = \boldsymbol{F}_0(\boldsymbol{v}_\mathrm{r}, \boldsymbol{\omega}, \boldsymbol{\delta}) + \boldsymbol{F}_v(\boldsymbol{v}_\mathrm{r}, \boldsymbol{\omega}, \boldsymbol{\delta})\boldsymbol{v}_\mathrm{r} \\ + \boldsymbol{F}_\omega(\boldsymbol{v}_\mathrm{r}, \boldsymbol{\omega}, \boldsymbol{\delta})\boldsymbol{\omega} + \text{H.O.T.}\end{aligned} \quad (40)$$

Assuming the estimate $\hat{\boldsymbol{v}}_\mathrm{r}$ is sufficiently close to $\boldsymbol{v}_\mathrm{r}$, the higher-order terms can be neglected so that the "known" signals $\boldsymbol{F}_{(\cdot)}$ in Assumption 2 are obtained by setting

$$\begin{aligned}\boldsymbol{F}_v(t) &= \left.\frac{\partial \boldsymbol{F}(\boldsymbol{v}_\mathrm{r}, \boldsymbol{\omega}(t), \boldsymbol{\delta}(t))}{\partial \boldsymbol{v}_\mathrm{r}}\right|_{\boldsymbol{v}_\mathrm{r} = \hat{\boldsymbol{v}}_\mathrm{r}(t)} \\ \boldsymbol{F}_\omega(t) &= \left.\frac{\partial \boldsymbol{F}(\hat{\boldsymbol{v}}_\mathrm{r}(t), \boldsymbol{\omega}, \boldsymbol{\delta}(t))}{\partial \boldsymbol{\omega}}\right|_{\boldsymbol{\omega} = \boldsymbol{\omega}(t)} \\ \boldsymbol{F}_0(t) &= \boldsymbol{F}(\hat{\boldsymbol{v}}_\mathrm{r}(t), \boldsymbol{\omega}(t), \boldsymbol{\delta}(t)) - \boldsymbol{F}_v(t)\hat{\boldsymbol{v}}_\mathrm{r} - \boldsymbol{F}_\omega(t)\boldsymbol{\omega}\end{aligned} \quad (41)$$

The force model error incurred by assuming $\boldsymbol{v}_{\mathrm{r}} - \hat{\boldsymbol{v}}_{\mathrm{r}} \approx \mathbf{0}$ is captured by the higher-order terms in Eq. (40). Furthermore, the quasi-steady, nonlinear force model $\boldsymbol{F}(\boldsymbol{v}_{\mathrm{r}}, \boldsymbol{\omega}, \boldsymbol{\delta})$ differs from the true force $\boldsymbol{F}_{\mathrm{true}}$ by unmodeled dynamics, parametric error, and wind gradients on the scale of the aircraft. Thus,

$$\Delta\boldsymbol{F} = \boldsymbol{F}_{\mathrm{true}} - \boldsymbol{F}(\hat{\boldsymbol{v}}_{\mathrm{r}}, \boldsymbol{\omega}, \boldsymbol{\delta}) \tag{42}$$

is the total force modeling error that perturbs the invariant error dynamics (32). The decomposition defined by Eq. (41) and the total modeling error in Eq. (42) are similarly defined for the moment $\boldsymbol{M}$. An additional source of error is the violation of Assumption 1 with the fact that $\dot{\boldsymbol{w}} \neq \mathbf{0}$. Thus, $\boldsymbol{d} = (\dot{\boldsymbol{w}}, \Delta\boldsymbol{M}, \Delta\boldsymbol{F})$ is the total disturbance to the invariant error dynamics (32) comprises turbulence and aerodynamic modeling error.

Including the disturbance $\boldsymbol{d}$ in the invariant error dynamics (33) reveals a method for selecting the $\boldsymbol{Q}$ and $\boldsymbol{R}$ matrices in the Riccati equation (36). That is, they may be selected in a manner similar to the Kalman-Bucy filter. The stochastic implications of this perspective are considered in detail in Ref. [35]. Considering turbulence and aerodynamic modeling error, Eq. (33) becomes

$$\dot{\boldsymbol{\eta}} = \big(\boldsymbol{A}(t) - \boldsymbol{L}(t)\boldsymbol{C}(t)\big)\boldsymbol{\eta} + \big(\boldsymbol{B}(t) - \boldsymbol{L}(t)\boldsymbol{D}(t)\big)\boldsymbol{d} \tag{43}$$

where

$$\boldsymbol{B}(t) = \begin{bmatrix} \boldsymbol{R}_{\mathrm{IB}}^{\mathsf{T}}(t) & \mathbf{0} & -\frac{1}{m}\mathbb{I} \\ -\boldsymbol{R}_{\mathrm{IB}}^{\mathsf{T}}(t) & \mathbf{0} & \mathbf{0} \end{bmatrix}, \quad \boldsymbol{D} = \begin{bmatrix} \mathbf{0} & \mathbf{0} & \mathbf{0} \\ \mathbf{0} & -\boldsymbol{I}^{-1} & \mathbf{0} \end{bmatrix} \tag{44.I}$$

$$\boldsymbol{B}(t) = \begin{bmatrix} \mathbb{I} & \mathbf{0} & -\frac{1}{m}\boldsymbol{R}_{\mathrm{IB}}(t) \\ -\mathbb{I} & \mathbf{0} & \mathbf{0} \end{bmatrix}, \quad \boldsymbol{D}(t) = \begin{bmatrix} \mathbf{0} & \mathbf{0} & \mathbf{0} \\ \mathbf{0} & -\boldsymbol{R}_{\mathrm{IB}}(t)\boldsymbol{I}^{-1} & \mathbf{0} \end{bmatrix} \tag{44.B}$$

Now, the gain design problem is to construct a full-order observer for the fictitious system

$$\dot{\boldsymbol{\xi}} = \boldsymbol{A}(t)\boldsymbol{\xi} + \boldsymbol{B}(t)\boldsymbol{d} \tag{45a}$$

$$\boldsymbol{\zeta} = \boldsymbol{C}(t)\boldsymbol{\xi} + \boldsymbol{D}(t)\boldsymbol{d} \tag{45b}$$

Under the assumption that $\boldsymbol{d}$ is zero-mean continuous-time white noise, Eq. (43) reveals that the solution to the gain design problem is *almost* the standard Kalman-Bucy filter. The only barrier is that $\boldsymbol{D}$ has rows of zeros, meaning some of the artificial outputs $\boldsymbol{\zeta}$ are noise-free. Since we are constrained to the closed loop error dynamics (43) and cannot consider more general formulations (e.g., taking derivatives of the noise-free output [36]), we consider a blended approach to tuning which does not necessarily produce an optimal estimate, but still will provide desirable performance. First, notice the structures of $\boldsymbol{B}$ and $\boldsymbol{D}$ imply that the components of $\boldsymbol{d}$ entering Eqs. (45a) and (45b) are distinct; that is, the "process noise" and "measurement noise" in Eq. (45) are uncorrelated. Accordingly, let

$$\bar{\boldsymbol{B}}(t) = \begin{bmatrix} \boldsymbol{R}_{\mathrm{IB}}^{\mathsf{T}}(t) & -\frac{1}{m}\mathbb{I} \\ -\boldsymbol{R}_{\mathrm{IB}}^{\mathsf{T}}(t) & \mathbf{0} \end{bmatrix}, \quad \bar{\boldsymbol{D}} = \begin{bmatrix} \mathbf{0} \\ -\boldsymbol{I}^{-1} \end{bmatrix} \tag{46.I}$$

$$\bar{\boldsymbol{B}}(t) = \begin{bmatrix} \mathbb{I} & -\frac{1}{m}\boldsymbol{R}_{\mathrm{IB}}(t) \\ -\mathbb{I} & \mathbf{0} \end{bmatrix}, \quad \bar{\boldsymbol{D}}(t) = \begin{bmatrix} \mathbf{0} \\ -\boldsymbol{R}_{\mathrm{IB}}(t)\boldsymbol{I}^{-1} \end{bmatrix} \tag{46.B}$$

reflect the non-zero input channels of $\boldsymbol{B}$ and $\boldsymbol{D}$, respectively. To circumvent the rank deficiency of $\bar{\boldsymbol{D}}\bar{\boldsymbol{D}}^{\mathsf{T}}$, define

$$\boldsymbol{R}(t) = \begin{bmatrix} \bar{\boldsymbol{D}}(t) & \boldsymbol{\Gamma} \end{bmatrix} \begin{bmatrix} \bar{\boldsymbol{D}}(t) & \boldsymbol{\Gamma} \end{bmatrix}^{\mathsf{T}} \tag{47}$$

where $\boldsymbol{\Gamma} \in \mathbb{R}^{6\times 3}$ is a tuning parameter that ensures $\boldsymbol{R}$ is invertible. The matrix $\boldsymbol{\Gamma}$ can be treated as the magnitude of the additional lumped disturbance in Eq. (43) due to imperfect measurements of $\boldsymbol{q}$ and $\boldsymbol{\omega}$. If this disturbance was white noise, then the positive definite matrix $\boldsymbol{R}$ would be the power spectral density of an augmented measurement noise vector that enters Eq. (45b). The process noise in Eq. (45a) has the intensity

$$\boldsymbol{Q}(t) = \bar{\boldsymbol{B}}(t)\,\mathbf{diag}(\boldsymbol{Q}_w, \boldsymbol{Q}_F)\bar{\boldsymbol{B}}^{\mathsf{T}}(t) \tag{48}$$

where $\boldsymbol{Q}_w$ and $\boldsymbol{Q}_F$ are power spectral densities of $\dot{\boldsymbol{w}}$ and $\Delta\boldsymbol{F}$, respectively.

V. Flight Test Setup

A. Research Aircraft

The symmetry-preserving reduced-order wind observer was implemented for the eSPAARO fixed-wing UAV shown in Figure 3. The eSPAARO is a 12 ft. wingspan, 45 lb. small UAS designed

Fig. 3 The eSPAARO research aircraft.

and built by Virginia Tech's Nonlinear Systems Laboratory. The eSPAARO is an inverted V-tail design with a pusher propeller configuration. The aircraft control surfaces comprise two ruddervators and two ailerons. The eSPAARO is instrumented with a Cubepilot CubeBlue flight computer running PX4 firmware, along with a HERE4 RTK GNSS system. It is propelled by a 22×12 in. Advanced Precision Composites (APC) propeller mounted to a 500 W brushless motor. The propulsion system is electrically powered by a ten-cell lithium-ion battery; its avionics and servos are redundantly powered by a separate three-cell lithium-ion polymer battery. More information about the general approach to instrumentation, flight test, and data processing can be found in Refs. [37–39].

Two vaned air data units (ADUs)*, designed and manufactured by the Nonlinear Systems Laboratory, were mounted to the eSPAARO's wingtips to aid in wind estimate validation. The ADUs were not used as part of the proposed wind observer; they were only used for validation of wind estimates. Each ADU consists of two 3D-printed vanes attached to 4,096-bit PWM, magnetic rotary

*Documentation and further information for the version used in this work may be found in the Attritable-Air-Data repository release v1.0: `https://github.com/jwhgit01/Attritable-Air-Data/releases/tag/v1.0/`.

encoders that are sampled at a rate of 200 Hz by a microcontroller. The vane angles are sent to the autopilot over the CAN bus via a custom PX4 driver. The tip of the ADU is a 3D-printed Kiel probe connected to a DLVR-10 differential pressure sensor, also communicating with the autopilot over the CAN bus at a 50 Hz sample rate.

Let V, α, and β_f be the airspeed, angle-of-attack, and flank angle, respectively, reported by one of the ADUs. First, the angle-of-attack and flank angle data were low-pass filtered with a cutoff frequency of 10 Hz to filter out any structural dynamics of the wing. The autopilot supplied inertial velocity estimates $\boldsymbol{v}_{\mathrm{i}}$ (average standard deviation of $[0.01\ 0.01\ 0.005]^{\mathsf{T}}$ m/s), attitude estimates (average standard deviation of $[0.004\ 0.004\ 0.013]^{\mathsf{T}} \in \mathsf{T}_{\hat{\boldsymbol{R}}_{\mathrm{IB}}}\mathsf{SO}(3)$), and angular velocity measurements from the calibrated gyroscope (noise and bias removed). These signals were used to reconstruct the apparent wind velocity

$$\boldsymbol{w} = \boldsymbol{v}_{\mathrm{i}} - \boldsymbol{R}_{\mathrm{IB}}\left(\boldsymbol{v}_{\mathrm{ADU}} - \boldsymbol{\omega} \times \boldsymbol{r}_{\mathrm{ADU}}\right) \tag{49}$$

where

$$\boldsymbol{v}_{\mathrm{ADU}} = \boldsymbol{R}_{\mathrm{BW}}(\alpha, \beta)\boldsymbol{e}_1 V$$

is the air-relative velocity at the geometric center of the two ADU vanes located at $\boldsymbol{r}_{\mathrm{ADU}}$. The rotation matrix $\boldsymbol{R}_{\mathrm{BW}}(\alpha, \beta) = e^{-\boldsymbol{S}(\boldsymbol{e}_2)\alpha} e^{\boldsymbol{S}(\boldsymbol{e}_3)\beta}$, which maps free vectors from the wind frame to the body frame, is parameterized by the measured angle-of-attack α, and the sideslip angle $\beta = \tan^{-1}(\tan(\beta_f)\cos(\alpha))$. For the purpose of wind estimate validation, the apparent wind $\boldsymbol{w}$ was taken to be the average of the wind velocities reconstructed between the two ADUs. The accuracy of the reconstructed wind velocity was quantified by propagating measurement uncertainties through Eq. (49), following the method in Ref. [18]. For the eSPAARO, this analysis yielded standard deviations between 0.1 and 0.3 m/s, depending on the vehicle's heading relative to the prevailing wind direction.

B. System Identification

An aero-propulsive model for the eSPAARO was identified from flight data following the approach detailed by Simmons et al. [40]. Orthogonal phase-optimized multisine inputs [41–43] were used to simultaneously excite the aircraft's propulsion system and control surfaces to provide informative six degree-of-freedom motion data. Specifically, independent excitations were applied to the throttle, left ruddervator, right ruddervator, and linked ailerons. The frequency content of the control surface excitation was between 0.05 Hz and 1.875 Hz to effectively excite the modes of longitudinal and lateral-directional motion. The frequency content of the propulsion excitation signal was between 0.050 Hz and 0.675 Hz due to the lower bandwidth of the propulsion system.

The aerodynamic force $\boldsymbol{F} = [X\ Y\ Z]^{\mathsf{T}}$ and moment $\boldsymbol{M} = [\mathcal{L}\ \mathcal{M}\ \mathcal{N}]^{\mathsf{T}}$ in the body frame are expressed with non-dimensional force and moment coefficients

$$\begin{aligned} C_x &= \frac{X}{\bar{q}S}, \quad C_y = \frac{Y}{\bar{q}S}, \quad C_z = \frac{Z}{\bar{q}S} \\ C_l &= \frac{\mathcal{L}}{\bar{q}Sb}, \quad C_m = \frac{\mathcal{M}}{\bar{q}Sc}, \quad C_n = \frac{\mathcal{N}}{\bar{q}Sb} \end{aligned} \tag{50}$$

where $\bar{q}$ is dynamic pressure, S is the wing planform area, b is the wingspan, and c is the chord length of the rectangular wings. The candidate explanatory variables for the model were angle of attack α, angle of sideslip β, non-dimensional angular rates

$$\breve{p} = \frac{pb}{2V}, \quad \breve{q} = \frac{qc}{2V}, \quad \breve{r} = \frac{rb}{2V}$$

control surface deflections δv_{L}, δv_{R}, δa, centered inverse advance ratio

$$\mathcal{J}_c = \frac{\Omega D}{V} - \mathcal{J}_0$$

and non-dimensional angle of attack rate $\breve{\dot{\alpha}} = \dot{\alpha}c/(2V)$. Here, δv_{L} and δv_{R} are the left and right ruddervator deflections, δa is the aileron deflection, Ω is the propeller speed, D is the propeller diameter, and $\mathcal{J}_0 = 15.7$ is the nominal inverse advance ratio. All angular quantities are expressed in radians. Geometric and inertial properties for the eSPAARO, as configured for model identification, are given in Table 3.

An effective strategy used to efficiently develop model structures is a combination of multivariate orthogonal function (MOF) modeling [43, 44] and stepwise regression [43]. First, MOF modeling is executed for several separate flight maneuvers. The model structures developed from each flight maneuver are compared, and the model terms appearing in a majority of the maneuvers are retained in the model. As a final step, the MOF results are reviewed by an analyst using stepwise regression to assess whether to include or exclude fringe model terms. From flight data collected using the 4-input multisine excitation signal, it was found that the following model structure accurately predicted the vehicle's motion from the training data.

$$C_x = C_{x_\alpha}\alpha + C_{x_{\alpha^2}}\alpha^2 + C_{x_{\mathcal{J}_c}}\mathcal{J}_c + C_{x_{\mathcal{J}_c^2}}\mathcal{J}_c^2 + C_{x_0} \tag{51a}$$

$$C_y = C_{y_\beta}\beta + C_{y_r}\breve{r} + C_{y_{\delta v_{\mathrm{L}}}}\delta v_{\mathrm{L}} + C_{y_{\delta v_{\mathrm{R}}}}\delta v_{\mathrm{R}} + C_{y_0} \tag{51b}$$

$$C_z = C_{z_\alpha}\alpha + C_{z_q}\breve{q} + C_{z_{\dot{\alpha}}}\breve{\dot{\alpha}} + C_{z_0} \tag{51c}$$

$$C_l = C_{l_\beta}\beta + C_{l_p}\breve{p} + C_{l_r}\breve{r} + C_{l_{\delta a}}\delta a + C_{l_0} \tag{51d}$$

$$C_m = C_{m_\alpha}\alpha + C_{m_q}\breve{q} + C_{m_{\delta v_{\mathrm{L}}}}\delta v_{\mathrm{L}} + C_{m_{\delta v_{\mathrm{R}}}}\delta v_{\mathrm{R}} + C_{m_0} \tag{51e}$$

$$\begin{aligned} C_n = {} & C_{n_\beta}\beta + C_{n_p}\breve{p} + C_{n_r}\breve{r} + C_{n_{\delta a}}\delta a + C_{n_{\delta v_{\mathrm{L}}}}\delta v_{\mathrm{L}} \\ & + C_{n_{\delta v_{\mathrm{R}}}}\delta v_{\mathrm{R}} + C_{n_0} \end{aligned} \tag{51f}$$

Remark 2. *Including the non-dimensional angle of attack rate $\breve{\dot{\alpha}}$ improved the eSPAARO model fit, but this term was neglected in the wind observer implementation since it is not a function of the instantaneous air-relative velocity.*

Following the equation error approach to system identification [43], the dependent variables C_x, C_y, C_z, C_l, C_m, and C_n were computed from flight data using filtered accelerometer and gyroscope data as described in Refs. [39, 45]. Equating these measurements to the model structure in Eq. (51), least squares regression was used to find the parameter estimates given in Table 2 in Appendix B. The model's valid domain, given in Table 1, was defined to be the interval between the minimum and maximum explanatory values with outliers beyond 1.5 times the interquartile range removed (as typical of a box and whisker plot).

C. Selection of Observer Parameters

With $\boldsymbol{Q}$ and $\boldsymbol{R}$ defined by Eqs. (48) and (47), respectively, the practitioner needs only to determine the power spectral densities

Table 1 Valid domain of explanatory variables for the eSPAARO aerodynamic model

Variable	Min	Median	Max	Units
V	12.12	20.83	31.87	m/s
α	-9.36	-0.25	8.60	deg
β	-29.60	-3.83	21.62	deg
p	-38.37	-0.12	37.79	deg/s
q	-29.64	1.38	32.20	deg/s
r	-34.59	-2.15	28.55	deg/s
δv_{L}	-16.03	-0.57	15.30	deg
δv_{R}	-12.12	0.89	14.63	deg
δa	-5.92	0.04	6.45	deg
Ω	190.3	479.2	778.0	rad/s

$\boldsymbol{Q}_w$, $\boldsymbol{Q}_M$, and $\boldsymbol{Q}_F$ and select the tuning parameter $\boldsymbol{\Gamma}$. For the eSPAARO, these parameters were chosen using historical flight data. To include flight in various directions with respect to the wind, the cloverleaf maneuver shown in Figure 4 was used to numerically determine $\boldsymbol{Q}_w$, $\boldsymbol{Q}_M$, and $\boldsymbol{Q}_F$.

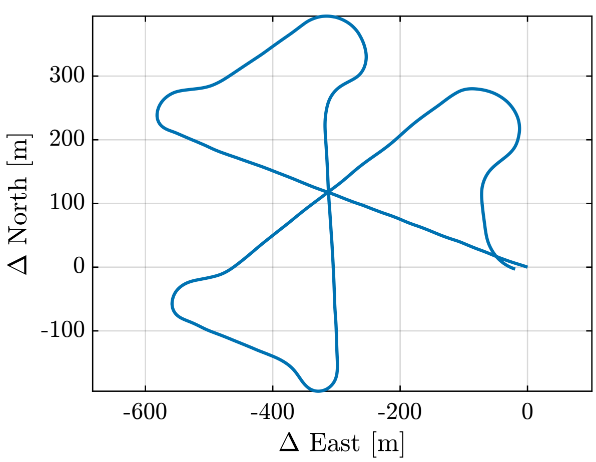

Fig. 4 Cloverleaf maneuver used for tuning.

Two different approaches may be used to determine the power spectral density of $\dot{\boldsymbol{w}}$. The first approach involves using some truth source, such as an air data unit or anemometer, to take a numerical derivative of the reconstructed wind $\boldsymbol{w}$. In practice, such specialized instrumentation is often available in the aircraft development process. The power spectral density of $\dot{\boldsymbol{w}}$ may be computed using `pwelch` in MATLAB, for instance. Then, $\boldsymbol{Q}_w$ is taken to be the maximum value of this power spectral density over all frequencies; that is, the colored noise $\dot{\boldsymbol{w}}$ is bounded by white noise with constant power spectral density $\boldsymbol{Q}_w$. The second approach, which was used to produce the results in this paper, begins by assuming the apparent wind is Brownian motion. Therefore, it should hold that

$$\operatorname{cov}\big(\boldsymbol{w}(t+\tau) - \boldsymbol{w}(t)\big) = \tau \boldsymbol{Q}_w \tag{52}$$

for any $\tau > 0$. Using the reconstructed wind, Eq. (52) can be used to compute $\boldsymbol{Q}_w$ for a variety of lag times τ. The final $\boldsymbol{Q}_w$ is then selected as its maximum value over all $\tau > 0$. For the aircraft and altitudes considered in this paper, $\boldsymbol{Q}_w$ was taken to be a diagonal matrix whose elements were selected from the results shown in Figure 5. Specifically,

$$\boldsymbol{Q}_w = \mathbf{diag}(0.96, 0.93, 1.38)\ \frac{(\mathrm{m/s})^2}{\mathrm{Hz}}$$

The benefit of this approach is that a numerical derivative of $\boldsymbol{w}$ is not needed to infer the power spectral density of $\dot{\boldsymbol{w}}$.

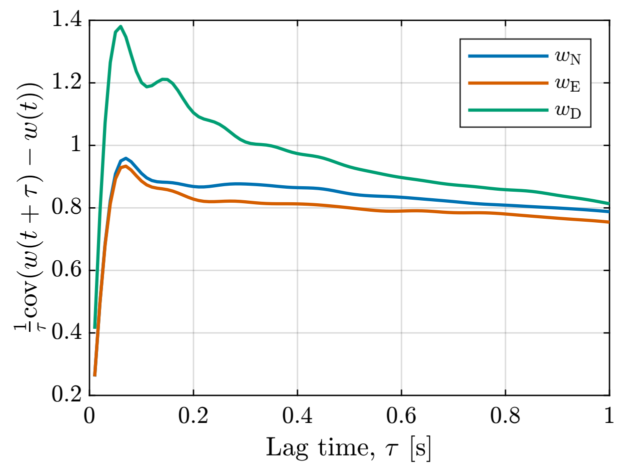

Fig. 5 Selection of $\boldsymbol{Q}_w$ through a Brownian motion assumption.

The power spectral densities of the force and moment modeling error signals $\Delta\boldsymbol{F}$ and $\Delta\boldsymbol{M}$ may be determined using a variety of methods. Here, we use the estimated aerodynamic model residual variance $\hat{\sigma}^2$ obtained through the system identification process for each force and moment component [43, Ch. 5]. The model error variance $\hat{\sigma}^2$ can be used to construct the power spectral density of the nonlinear model error $\boldsymbol{F}_{\mathrm{true}} - \boldsymbol{F}(\boldsymbol{v}_{\mathrm{r}}, \boldsymbol{\omega}, \boldsymbol{\delta})$, for instance. To accurately characterize the total modeling error $\Delta\boldsymbol{F}$, the additional perturbation $\Delta\hat{\boldsymbol{F}} = \boldsymbol{F}(\hat{\boldsymbol{v}}_{\mathrm{r}}, \boldsymbol{\omega}, \boldsymbol{\delta}) - \boldsymbol{F}(\boldsymbol{v}_{\mathrm{r}}, \boldsymbol{\omega}, \boldsymbol{\delta})$ must also be quantified. We recognize, however, that the term $\Delta\hat{\boldsymbol{F}}$ is a vanishing perturbation; that is, $\Delta\hat{\boldsymbol{F}} = \mathbf{0}$ when $\hat{\boldsymbol{v}}_{\mathrm{r}} = \boldsymbol{v}_{\mathrm{r}}$. Therefore, we choose to neglect $\Delta\hat{\boldsymbol{F}}$ when selecting the power spectral density $\boldsymbol{Q}_F$ (and similarly for $\boldsymbol{Q}_M$). From the system identification process described in Section V.B, the force and moment modeling error power spectral densities are

$$\boldsymbol{Q}_F = \mathbf{diag}(7.6, 14.1, 108.0)\ \frac{\mathrm{N}^2}{\mathrm{Hz}}$$

$$\boldsymbol{Q}_M = \mathbf{diag}(37.7, 19.9, 11.3)\ \frac{(\mathrm{N}\cdot\mathrm{m})^2}{\mathrm{Hz}}$$

Finally, the tuning parameter $\boldsymbol{\Gamma}$ was chosen to be $\boldsymbol{\Gamma} = [0.3\,\mathbb{I}\ \ \mathbf{0}]^{\mathsf{T}}$. This value was large enough to not cause over-amplification of measurement noise while still being small enough not to hinder the convergence rate of the observer.

Remark 3. *While $\Delta\hat{\boldsymbol{F}}$ is neglected in the above selection of $\boldsymbol{Q}_F$ due to its vanishing behavior when $\hat{\boldsymbol{v}}_{\mathrm{r}} = \boldsymbol{v}_{\mathrm{r}}$, one could incorporate it to improve performance or strengthen stability guarantees. Let $\tilde{v}_{\mathrm{r,max}}$ denote the maximum expected error in the air-relative velocity estimate corresponding to operational and performance limits. Then, using Monte-Carlo analysis over the model's valid domain (e.g., Table 1), the power spectral density of $\Delta\hat{\boldsymbol{F}}$ could be estimated and used to inform a more conservative choice of $\boldsymbol{Q}_F$.*

VI. Wind Estimation Results

To demonstrate the observer's large region of attraction, the automated S-turn maneuver shown in Figure 6 was performed. The apparent wind velocity was reconstructed using Eq. (49) and

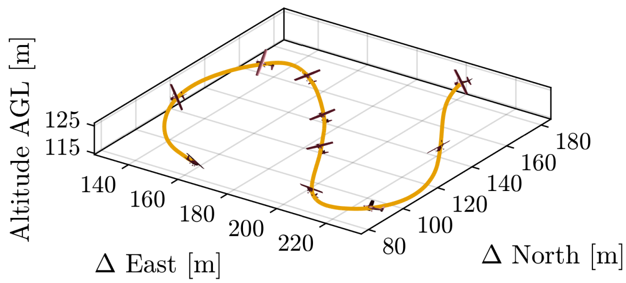

Fig. 6 Automated S-turn trajectory at 120 m above ground level (AGL).

is shown in Figure 7. During this maneuver, the prevailing wind

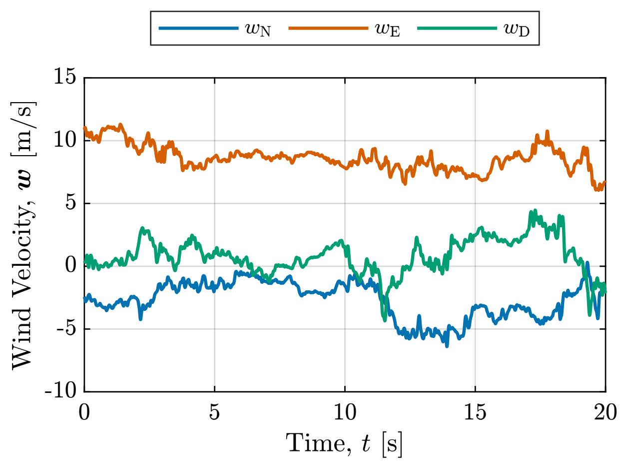

Fig. 7 Reconstructed wind velocity during S-turn maneuver.

averaged 9.1 m/s from 285 degrees (West-Northwest) with gusts up to 12 m/s.

Before implementing the observer on this maneuver, the observability condition of Theorem 3 was verified. The square LTV observability Gramian $\boldsymbol{G}_o(t_0, t_f)$ was numerically constructed backwards in time from $t_f = 20$ to $t_0 = 0$. As shown in Figure 8, the minimum eigenvalue of the observability Gramian is bounded away from zero backwards in time, implying observability of $(\boldsymbol{A}(t), \boldsymbol{C}(t))$ on the interval $[t_0, 20)$ for any $t_0 \geq 0$ [46, Ch. 9]. Due to the structure of $\boldsymbol{A}$ and $\boldsymbol{C}$, the minimum eigenvalue $\lambda_{\min}(\boldsymbol{G}_o)$ is the same for both transformation groups. Also shown in Figure 8 is the minimum eigenvalue of the observability Gramian for straight-and-level, steady flight in zero wind, showing that persistent maneuvering is not a requirement for the observability condition of Theorem 3 to hold.

A. Simulation Results

The symmetry-preserving reduced-order wind observers detailed in Section III were first implemented in simulation with all assumptions satisfied in order to demonstrate the theoretical convergence guarantees. That is, the aerodynamic force and moment satisfy Assumption 2, and the wind is constant to satisfy Assumption 1. For this ideal case, the eSPAARO aerodynamic model (51)

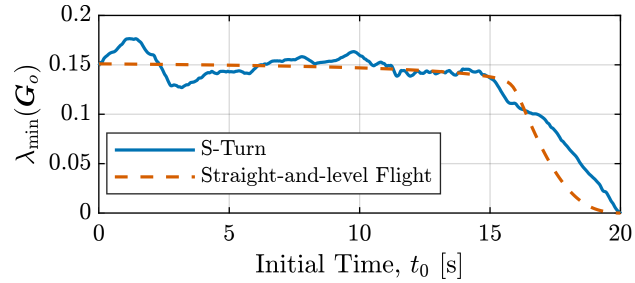

Fig. 8 Minimum eigenvalue of the LTV observability Gramian on the interval $[t_0, 20)$.

is decomposed according to Eq. (41), except with $\hat{\boldsymbol{v}}_{\mathrm{r}}(t) = \boldsymbol{v}_{\mathrm{r}}(t)$ so that the time-varying parameters $\boldsymbol{F}_{(\cdot)}, \boldsymbol{M}_{(\cdot)}$ are perfectly known. The aircraft dynamics (7) were simulated in a uniform wind field with constant components $W_{\mathrm{N}} = -2.69$ m/s, $W_{\mathrm{E}} = 8.62$ m/s, and $W_{\mathrm{D}} = 0.81$ m/s equal to the mean reconstructed wind during the flight test maneuver. For the simulation, a time-varying linear quadratic regulator was used to obtain a simulated trajectory the same as the S-turn flight data shown in Figure 6.

The observers for both the inertial and body transformation groups were implemented on the simulation data. The initial unmeasured state estimates corresponded to straight-and-level flight at 20 m/s in zero wind. Specifically, $\hat{\boldsymbol{w}}(0) = \boldsymbol{0}$ m/s and $\hat{\boldsymbol{v}}_{\mathrm{r}}(0) = [19.98\ 0\ 0.66]^{\mathsf{T}}$ m/s. Since all assumptions were satisfied, the observers designed using both transformation groups yielded very similar results, only differing in the initial transient behavior. This parity is expected since the same rotational symmetry of the dynamics is equivalently preserved — just from the viewpoint of different reference frames. The practical difference between using transformation groups (12.I) and (12.B) is the coordinate frame in which the observer mapping $\boldsymbol{\ell}$ and thus the Riccati equation (36) evolve. The estimates of air-relative and wind velocity are shown in Figures 9 and 10, respectively, demonstrating the guaranteed exponential convergence despite large variations in the aircraft's state.

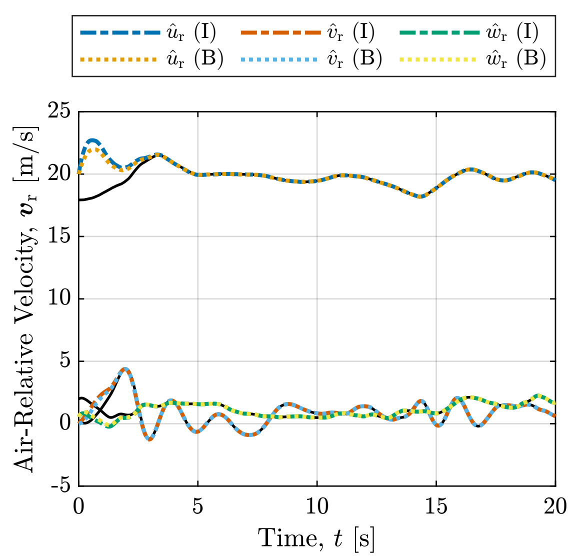

Fig. 9 Air-relative velocity estimates using the inertial (I) and body (B) transformation groups compared to simulation data (solid black line).

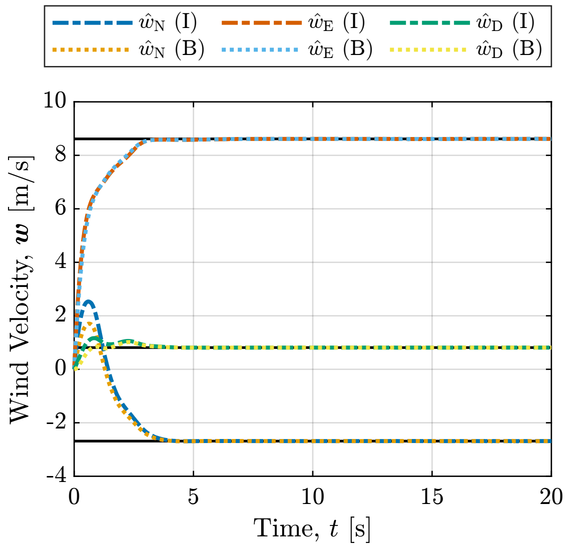

Fig. 10 Wind velocity estimates using the inertial (I) and body (B) transformation groups compared to simulation data (solid black line).

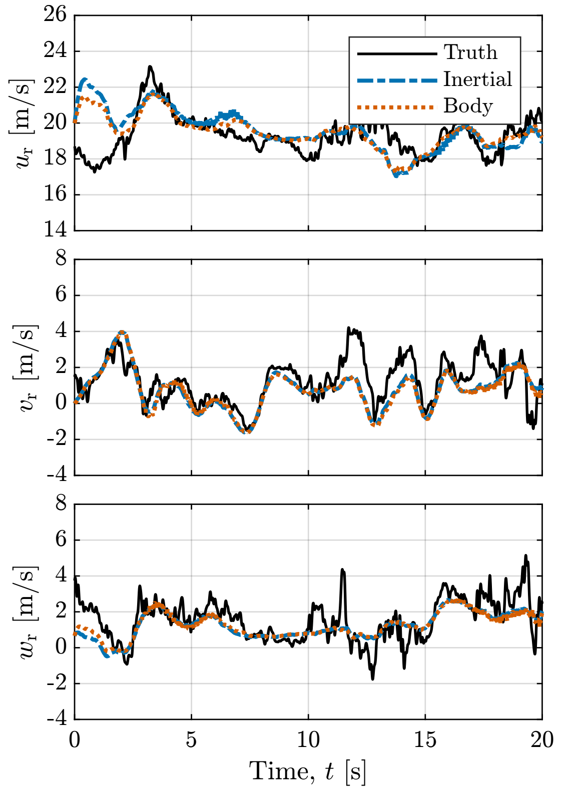

Fig. 11 Air-relative velocity estimates using the inertial and body transformation groups compared to flight data.

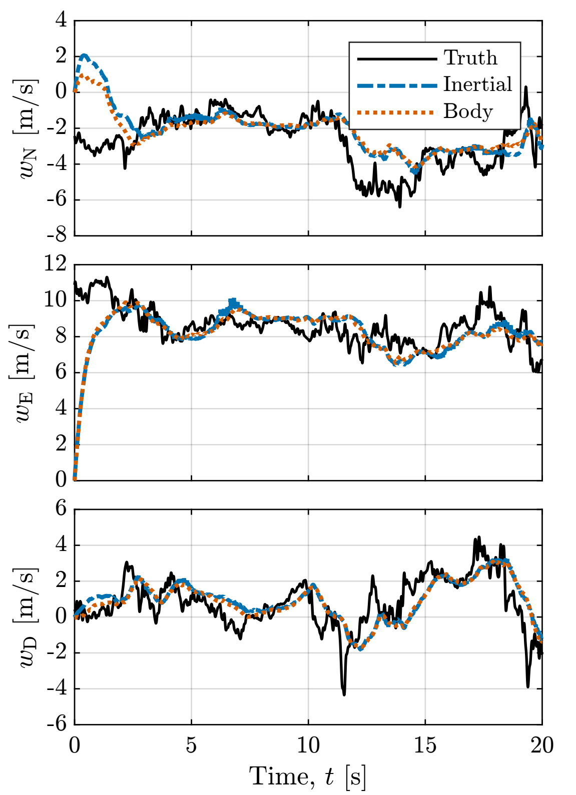

Fig. 12 Wind velocity estimates using the inertial and body transformation groups compared to flight data.

B. Flight Test Results

The simulation results in Section VI.A showcase the observer's guarantees under idealized assumptions on the wind field and the aircraft's aerodynamics. As discussed in Section IV, the true wind is not constant, and the aerodynamic force and moment models differ from the true force and moment by both unmodeled dynamics and parametric error. Critically, the symmetry-preserving reduced-order wind observer is locally robust to these sources of error since the undisturbed invariant error system is globally exponentially stable [47, Theorem 5.1]. By implementing the observer on flight data, we demonstrate this robustness — namely, sufficiently small wind fluctuations and aerodynamic modeling error yield norm-bounded state estimation error.

The symmetry-preserving reduced-order wind observer was implemented on the flight data using both the inertial and body transformation groups as done with the simulation data in Section VI.A. The components of the air-relative velocity and wind velocity estimates are shown in Figures 11 and 12, respectively. For the S-turn maneuver, the observer's performance is similar between the two transformation groups. However, the observer synthesized using the inertial transformation group exhibits minor noise amplification, visible in the east wind velocity estimates around 7 seconds into the maneuver (Figure 12). The state estimate root mean square error

$$\mathrm{RMSE}(\boldsymbol{x}) = \left(\frac{1}{t_f - t_0} \int_{t_0}^{t_f} \|\hat{\boldsymbol{x}}(t) - \boldsymbol{x}(t)\|^2 \mathrm{d}t \right)^{\frac{1}{2}} \tag{53}$$

was also computed to quantify the small difference between transformation groups. For the S-turn, the inertial transformation group yielded $\mathrm{RMSE}(\boldsymbol{x}) = 1.59$ m/s, whereas the body transformation group resulted in $\mathrm{RMSE}(\boldsymbol{x}) = 1.55$ m/s.

To further investigate performance and robustness differences between the two transformation groups, the observer was implemented on the cloverleaf maneuver used to determine $\boldsymbol{Q}_w$, $\boldsymbol{Q}_F$, and $\boldsymbol{Q}_M$ as described in Section V.C. The observer's poorest performance occurred around 48 seconds from the start of this maneuver, where the aircraft sharply executes a right-hand turn. As seen in Figure 13, the observer designed using the inertial transformation group produces rather large estimation error. The

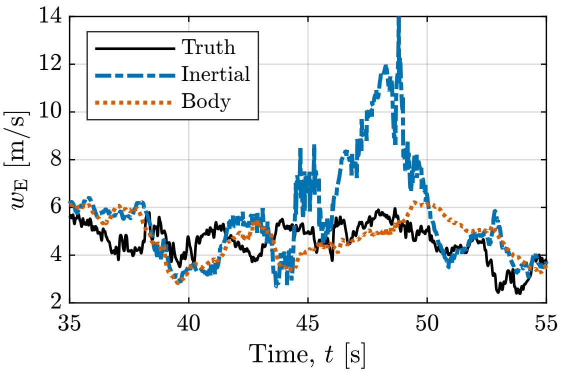

Fig. 13 Comparison of transformation groups for east wind velocity estimates during the first turn of the cloverleaf maneuver.

observer designed using the body transformation group is more robust to the modeling errors and measurement perturbations that occurred during this turn. The radius of curvature for the turns in the cloverleaf maneuver was much smaller than the S-turn, resulting in aileron deflections and roll rates well beyond the model's valid domain given in Table 1. During the 20 seconds shown in Figure 13, the root mean square error using the inertial transformation group was $\mathrm{RMSE}(\boldsymbol{x}) = 1.80$ m/s, whereas the body transformation group resulted in much smaller error with $\mathrm{RMSE}(\boldsymbol{x}) = 1.45$ m/s.

The symmetry-preserving wind observer was also compared to a continuous-discrete extended Kalman filter (EKF) constituting a baseline full-order filtering approach. The EKF assumed the same process model (7) as the symmetry-preserving observer. Thus, the sources of process noise are the same between these two approaches. The same measurements were assumed (position, attitude, and angular velocity), except that discrete-time measurement noise was considered in the formulation of the EKF. The measurement noise covariance matrices for position and attitude were taken to be the average state estimation error covariance reported by the autopilot's navigation solution. From the cloverleaf maneuver, these are

$$\boldsymbol{P}_q = \mathbf{diag}\,(0.027,\ 0.027,\ 0.039)\ \mathrm{m}^2$$
$$\boldsymbol{P}_{R_{\mathrm{IB}}} = \mathbf{diag}\,(1.54, 1.54, 16.6) \times 10^{-5}$$

where $\boldsymbol{P}_{R_{\mathrm{IB}}}$ is the covariance of the attitude estimate error in $\mathsf{T}_{\hat{\boldsymbol{R}}_{\mathrm{IB}}}\mathsf{SO}(3)$. The angular velocity measurement noise was characterized by comparing raw to smoothed gyroscope data; it's power spectral density was found to be

$$\boldsymbol{Q}_{\mathrm{gyro}} = \mathbf{diag}\,(2.18, 1.05, 0.04) \times 10^{-4}\ \frac{(\mathrm{rad/s})^2}{\mathrm{Hz}}$$

Thus, the discrete-time measurement noise covariance for the EKF is

$$\boldsymbol{R} = \mathbf{diag}\,(\boldsymbol{P}_q, \boldsymbol{P}_{R_{\mathrm{IB}}}, \boldsymbol{Q}_{\mathrm{gyro}}/\Delta t) \tag{54}$$

where Δt is the time between measurements.

As a representative example, the east wind velocity estimates using the EKF are shown in Figure 14 along with the symmetry-preserving observer synthesized using the body transformation group. The EKF achieves performance comparable

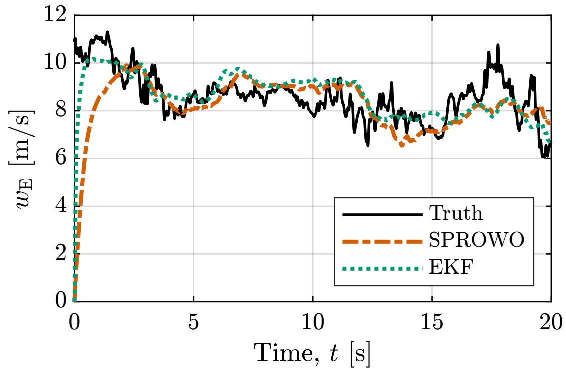

Fig. 14 Comparison of the symmetry-preserving reduced-order wind observer (SPROWO) using the body transformation group with a continuous-discrete extended Kalman filter (EKF).

to the symmetry-preserving reduced-order observer, with a root mean square error of $\mathrm{RMSE}(\boldsymbol{x}) = 1.46$ m/s. The main difference lies in the initial transients, where the EKF exhibits a faster convergence. This difference is attributed to the tuning parameter $\boldsymbol{\Gamma}$. As discussed in Section IV, choosing a smaller $\boldsymbol{\Gamma}$ increases the convergence rate of the reduced-order observer but also amplifies measurement noise. It is worth emphasizing, however, that unlike the symmetry-preserving reduced-order observer, the EKF does not offer guaranteed performance.

VII. Conclusions

A symmetry-preserving, reduced-order observer has been applied to the problem of wind estimation from aircraft motion. The proposed observer does not rely on a small-perturbation assumption, but rather exploits the invariance of the aircraft dynamics under rotations to ensure exponential convergence of the estimate. Furthermore, the reduced-order formulation does not re-estimate known parts of the state vector, reducing computational complexity and simplifying tuning. The observer's theoretical guarantees are demonstrated through simulation of a nonlinear fixed-wing aircraft model. Observers synthesized using both body-frame and inertial-frame transformation groups yielded comparable results as expected. In the flight test results, however, it was found that the body-frame transformation group yielded more robust wind estimates. Applying the observers to flight data demonstrated the observer's practical utility and robustness to aerodynamic modeling error and unmodeled turbulence. While a uniform and steady wind field is assumed for the design of the observer, the approach also performs well in the presence of wind fluctuations — a robustness afforded by the global exponential stability guarantees on the invariant error dynamics. Overall, this provably stable observer provides strong guarantees that can be incorporated into a wide variety of applications, such as synthetic air data systems, path planning algorithms, safety monitoring solutions, and numerical weather models.

A. Proof of Proposition 1

Note that the tangent maps of the transformation groups (12.I) and (12.B) at $(\boldsymbol{x},\boldsymbol{y},\boldsymbol{u})$ applied to $\boldsymbol{f}(\boldsymbol{x},\boldsymbol{y},\boldsymbol{u})$ and $\boldsymbol{h}(\boldsymbol{x},\boldsymbol{y},\boldsymbol{u})$ respectively satisfy

$$\mathrm{T}_{\boldsymbol{x}}\boldsymbol{\varphi}_g\big(\boldsymbol{f}(\boldsymbol{x},\boldsymbol{y},\boldsymbol{u})\big)=\begin{pmatrix}\boldsymbol{f}_{v_{\mathrm{r}}}(\boldsymbol{x},\boldsymbol{u})\\ \boldsymbol{R}_g\boldsymbol{f}_w(\boldsymbol{x},\boldsymbol{u})\end{pmatrix}\quad\text{and}$$

$$\mathrm{T}_{\boldsymbol{y}}\boldsymbol{\varrho}_g\big(\boldsymbol{h}(\boldsymbol{x},\boldsymbol{y},\boldsymbol{u})\big)=\begin{pmatrix}\boldsymbol{R}_g\boldsymbol{f}_q(\boldsymbol{x},\boldsymbol{u})\\ \boldsymbol{R}_g\boldsymbol{f}_{R_{\mathrm{IB}}}(\boldsymbol{x},\boldsymbol{u})\\ \boldsymbol{f}_\omega(\boldsymbol{x},\boldsymbol{u})\end{pmatrix}\tag{A.1.I}$$

$$\mathrm{T}_{\boldsymbol{x}}\boldsymbol{\varphi}_g\big(\boldsymbol{f}(\boldsymbol{x},\boldsymbol{y},\boldsymbol{u})\big)=\begin{pmatrix}\boldsymbol{R}_g\boldsymbol{f}_{v_{\mathrm{r}}}(\boldsymbol{x},\boldsymbol{u})\\ \boldsymbol{f}_w(\boldsymbol{x},\boldsymbol{u})\end{pmatrix}\quad\text{and}$$

$$\mathrm{T}_{\boldsymbol{y}}\boldsymbol{\varrho}_g\big(\boldsymbol{h}(\boldsymbol{x},\boldsymbol{y},\boldsymbol{u})\big)=\begin{pmatrix}\boldsymbol{f}_q(\boldsymbol{x},\boldsymbol{u})\\ \boldsymbol{f}_{R_{\mathrm{IB}}}(\boldsymbol{x},\boldsymbol{u})\boldsymbol{R}_g^{\mathsf{T}}\\ \boldsymbol{R}_g\boldsymbol{f}_\omega(\boldsymbol{x},\boldsymbol{u})\end{pmatrix}\tag{A.1.B}$$

We must show that the expressions above are equal to the evaluation of $\boldsymbol{f}$ and $\boldsymbol{h}$ at the transformed point $(\boldsymbol{\varphi}_g(\boldsymbol{x}),\boldsymbol{\varrho}_g(\boldsymbol{u}),\boldsymbol{\psi}_g(\boldsymbol{u}))$. Starting with the relative velocity dynamics, we have

$$\begin{aligned}\boldsymbol{f}_{v_{\mathrm{r}}}(\boldsymbol{\varphi}_g(\boldsymbol{x}),\boldsymbol{\varrho}_g(\boldsymbol{y}),\boldsymbol{\psi}_g(\boldsymbol{u}))&=\boldsymbol{v}_{\mathrm{r}}\times\boldsymbol{\omega}+\boldsymbol{R}_{\mathrm{IB}}^{\mathsf{T}}\boldsymbol{R}_g^{\mathsf{T}}\boldsymbol{R}_g\boldsymbol{g}\\&\quad+\tfrac{1}{m}\left(\boldsymbol{F}_0+\boldsymbol{F}_v\boldsymbol{v}_{\mathrm{r}}+\boldsymbol{F}_\omega\boldsymbol{\omega}\right)\\&=\boldsymbol{f}_{v_{\mathrm{r}}}(\boldsymbol{x},\boldsymbol{y},\boldsymbol{u})\end{aligned}\tag{A.2.I}$$

$$\begin{aligned}\boldsymbol{f}_{v_{\mathrm{r}}}(\boldsymbol{\varphi}_g(\boldsymbol{x}),\boldsymbol{\varrho}_g(\boldsymbol{y}),\boldsymbol{\psi}_g(\boldsymbol{u}))&=\boldsymbol{R}_g\boldsymbol{v}_{\mathrm{r}}\times\boldsymbol{R}_g\boldsymbol{\omega}+\boldsymbol{R}_g\boldsymbol{R}_{\mathrm{IB}}^{\mathsf{T}}\boldsymbol{g}\\&\quad+\frac{1}{m}\left(\boldsymbol{R}_g\boldsymbol{F}_0+\boldsymbol{R}_g\boldsymbol{F}_v\boldsymbol{R}_g^{\mathsf{T}}\boldsymbol{R}_g\boldsymbol{v}_{\mathrm{r}}+\boldsymbol{R}_g\boldsymbol{F}_\omega\boldsymbol{R}_g^{\mathsf{T}}\boldsymbol{R}_g\boldsymbol{\omega}\right)\\&=\boldsymbol{R}_g\left(\boldsymbol{v}_{\mathrm{r}}\times\boldsymbol{\omega}+\boldsymbol{R}_{\mathrm{IB}}^{\mathsf{T}}\boldsymbol{g}+\tfrac{1}{m}\left(\boldsymbol{F}_0+\boldsymbol{F}_v\boldsymbol{v}_{\mathrm{r}}+\boldsymbol{F}_\omega\boldsymbol{\omega}\right)\right)\\&=\boldsymbol{R}_g\boldsymbol{f}_{v_{\mathrm{r}}}(\boldsymbol{x},\boldsymbol{y},\boldsymbol{u})\end{aligned}\tag{A.2.B}$$

The invariance of the apparent wind velocity dynamics $\dot{\boldsymbol{w}}=\boldsymbol{0}$ is trivially satisfied. For the position kinematics, we write

$$\boldsymbol{f}_q(\boldsymbol{\varphi}_g(\boldsymbol{x}),\boldsymbol{\varrho}_g(\boldsymbol{y}),\boldsymbol{\psi}_g(\boldsymbol{u}))=\boldsymbol{R}_g\boldsymbol{R}_{\mathrm{IB}}\boldsymbol{v}_{\mathrm{r}}+\boldsymbol{R}_g\boldsymbol{w}=\boldsymbol{R}_g\boldsymbol{f}_q(\boldsymbol{x},\boldsymbol{y},\boldsymbol{u})\tag{A.3.I}$$

$$\boldsymbol{f}_q(\boldsymbol{\varphi}_g(\boldsymbol{x}),\boldsymbol{\varrho}_g(\boldsymbol{y}),\boldsymbol{\psi}_g(\boldsymbol{u}))=\boldsymbol{R}_{\mathrm{IB}}\boldsymbol{R}_g^{\mathsf{T}}\boldsymbol{R}_g\boldsymbol{v}_{\mathrm{r}}+\boldsymbol{w}=\boldsymbol{f}_q(\boldsymbol{x},\boldsymbol{y},\boldsymbol{u})\tag{A.3.B}$$

The attitude kinematics at the transformed point satisfy

$$\boldsymbol{f}_{R_{\mathrm{IB}}}(\boldsymbol{\varphi}_g(\boldsymbol{x}),\boldsymbol{\varrho}_g(\boldsymbol{y}),\boldsymbol{\psi}_g(\boldsymbol{u}))=\boldsymbol{R}_g\boldsymbol{R}_{\mathrm{IB}}\boldsymbol{S}(\boldsymbol{\omega})=\boldsymbol{R}_g\boldsymbol{f}_{R_{\mathrm{IB}}}(\boldsymbol{x},\boldsymbol{y},\boldsymbol{u})\tag{A.4.I}$$

$$\begin{aligned}\boldsymbol{f}_{R_{\mathrm{IB}}}(\boldsymbol{\varphi}_g(\boldsymbol{x}),\boldsymbol{\varrho}_g(\boldsymbol{y}),\boldsymbol{\psi}_g(\boldsymbol{u}))&=\boldsymbol{R}_{\mathrm{IB}}\boldsymbol{R}_g^{\mathsf{T}}\boldsymbol{S}(\boldsymbol{R}_g\boldsymbol{\omega})\\&=\boldsymbol{R}_{\mathrm{IB}}\boldsymbol{R}_g^{\mathsf{T}}\boldsymbol{R}_g\boldsymbol{S}(\boldsymbol{\omega})\boldsymbol{R}_g^{\mathsf{T}}\\&=\boldsymbol{f}_{R_{\mathrm{IB}}}(\boldsymbol{x},\boldsymbol{y},\boldsymbol{u})\boldsymbol{R}_g^{\mathsf{T}}\end{aligned}\tag{A.4.B}$$

In the second line of Eq. (A.4.B), we have used the property that $\boldsymbol{S}(\boldsymbol{R}\boldsymbol{\omega})=\boldsymbol{R}\boldsymbol{S}(\boldsymbol{\omega})\boldsymbol{R}^{\mathsf{T}}$ for any $\boldsymbol{R}\in\mathsf{SO}(3)$ and $\boldsymbol{\omega}\in\mathbb{R}^3$. Finally, the angular velocity dynamics are invariant since

$$\begin{aligned}\boldsymbol{f}_\omega(\boldsymbol{\varphi}_g(\boldsymbol{x}),\boldsymbol{\varrho}_g(\boldsymbol{y}),\boldsymbol{\psi}_g(\boldsymbol{u}))&=\boldsymbol{I}^{-1}(\boldsymbol{I}\boldsymbol{\omega}\times\boldsymbol{\omega}+\boldsymbol{M}_0+\boldsymbol{M}_v\boldsymbol{v}_{\mathrm{r}}+\boldsymbol{M}_\omega\boldsymbol{\omega})\\&=\boldsymbol{f}_\omega(\boldsymbol{x},\boldsymbol{y},\boldsymbol{u})\end{aligned}\tag{A.5.I}$$

$$\begin{aligned}\boldsymbol{f}_\omega(\boldsymbol{\varphi}_g(\boldsymbol{x}),\boldsymbol{\varrho}_g(\boldsymbol{y}),\boldsymbol{\psi}_g(\boldsymbol{u}))&=\left(\boldsymbol{R}_g\boldsymbol{I}\boldsymbol{R}_g^{\mathsf{T}}\right)^{-1}\big(\boldsymbol{R}_g\boldsymbol{I}\boldsymbol{R}_g^{\mathsf{T}}\boldsymbol{R}_g\boldsymbol{\omega}\times\boldsymbol{R}_g\boldsymbol{\omega}\\&\quad+\boldsymbol{R}_g\boldsymbol{M}_0+\boldsymbol{R}_g\boldsymbol{M}_v\boldsymbol{R}_g^{\mathsf{T}}\boldsymbol{R}_g\boldsymbol{v}_{\mathrm{r}}+\boldsymbol{R}_g\boldsymbol{M}_\omega\boldsymbol{R}_g^{\mathsf{T}}\boldsymbol{R}_g\boldsymbol{\omega}\big)\\&=\boldsymbol{R}_g\boldsymbol{I}^{-1}\left(-\boldsymbol{S}(\boldsymbol{\omega})\boldsymbol{I}\boldsymbol{\omega}+\boldsymbol{M}_0+\boldsymbol{M}_v\boldsymbol{v}_{\mathrm{r}}+\boldsymbol{M}_\omega\boldsymbol{\omega}\right)\\&=\boldsymbol{R}_g\boldsymbol{f}_\omega(\boldsymbol{x},\boldsymbol{y},\boldsymbol{u})\end{aligned}\tag{A.5.B}$$

Therefore, the tangent maps (A.1) satisfy the statement (11) of G-invariance. □

B. Aerodynamic Model Parameters

The eSPAARO aerodynamic model parameters, appearing in Eq. (51), are given in Table 2. The aircraft's geometric and inertial properties are given in Table 3.

Table 2 Parameter estimates for the eSPAARO aerodynamic model

Parameter	Estimate	Std. Dev.
C_{x_α}	2.16×10^{-1}	1.44×10^{-2}
$C_{x_{\alpha^2}}$	1.94	1.78×10^{-1}
$C_{x_{\mathcal{J}_c}}$	2.10×10^{-2}	2.02×10^{-4}
$C_{x_{\mathcal{J}_c^2}}$	6.07×10^{-4}	3.57×10^{-5}
C_{x_0}	5.93×10^{-2}	3.93×10^{-3}
C_{y_β}	-3.53×10^{-1}	1.13×10^{-2}
C_{y_r}	1.29×10^{-1}	3.51×10^{-2}
$C_{y_{\delta v_{\mathrm{L}}}}$	-7.58×10^{-2}	6.97×10^{-3}
$C_{y_{\delta v_{\mathrm{R}}}}$	8.16×10^{-2}	7.32×10^{-3}
C_{y_0}	-2.99×10^{-2}	9.63×10^{-4}
C_{z_α}	-3.43	2.53×10^{-1}
C_{z_q}	-1.09×10^{1}	3.11
$C_{z_{\dot\alpha}}$	1.63×10^{1}	3.21
C_{z_0}	-6.10×10^{-1}	2.55×10^{-2}
C_{l_β}	7.71×10^{-3}	3.60×10^{-3}
C_{l_p}	-4.22×10^{-1}	1.71×10^{-2}
C_{l_r}	1.29×10^{-1}	1.10×10^{-2}
$C_{l_{\delta a}}$	-2.75×10^{-1}	9.41×10^{-3}
C_{l_0}	7.99×10^{-4}	9.09×10^{-5}
C_{m_α}	-5.38×10^{-1}	4.93×10^{-2}
C_{m_q}	-1.01×10^{1}	7.11×10^{-1}
$C_{m_{\delta v_{\mathrm{L}}}}$	-4.41×10^{-1}	1.55×10^{-2}
$C_{m_{\delta v_{\mathrm{R}}}}$	-4.80×10^{-1}	1.66×10^{-2}
C_{m_0}	-1.87×10^{-3}	1.10×10^{-3}
C_{n_β}	7.90×10^{-2}	1.86×10^{-3}
C_{n_p}	-4.05×10^{-2}	8.81×10^{-3}
C_{n_r}	-5.91×10^{-2}	5.90×10^{-3}
$C_{n_{\delta a}}$	1.48×10^{-2}	4.82×10^{-3}
$C_{n_{\delta v_{\mathrm{L}}}}$	3.83×10^{-2}	1.16×10^{-3}
$C_{n_{\delta v_{\mathrm{R}}}}$	-3.59×10^{-2}	1.20×10^{-3}
C_{n_0}	-1.82×10^{-3}	2.69×10^{-4}

Table 3 Inertial and geometric properties of the eSPAARO

Property	Value	Units
m	20.43	kg
I_{xx}	7.41	$\mathrm{kg\cdot m^2}$
I_{yy}	8.50	$\mathrm{kg\cdot m^2}$
I_{zz}	12.73	$\mathrm{kg\cdot m^2}$
I_{xz}	0.18	$\mathrm{kg\cdot m^2}$
c	0.559	m
b	3.658	m
S	2.044	$\mathrm{m^2}$
D	0.559	m

Acknowledgments

The authors gratefully acknowledge NASA under Grant No. 80NSSC20M0162. The authors also thank Garrett Asper, Patrick Corrigan, and Samuel Widman for flight test support.

References

[1] Lie, F. A. P., and Gebre-Egziabher, D., "Synthetic air data system," *Journal of Aircraft*, Vol. 50, No. 4, 2013, pp. 1234–1249. https://doi.org/10.2514/1.C032177.

[2] Sun, K., Regan, C. D., and Gebre-Egziabher, D., "Observability and performance analysis of a model-free synthetic air data estimator," *Journal of Aircraft*, Vol. 56, No. 4, 2019, pp. 1471–1486. https://doi.org/10.2514/1.C035290.

[3] Lawrance, N. R., and Sukkarieh, S., "Path planning for autonomous soaring flight in dynamic wind fields," *2011 IEEE International Conference on Robotics and Automation*, IEEE, Shanghai, China, 2011, pp. 2499–2505. https://doi.org/10.1109/ICRA.2011.5979966.

[4] Yang, S., and Jeon, S., "Recursive path planning and wind field estimation for precision airdrop," *Journal of Guidance, Control, and Dynamics*, Vol. 42, No. 6, 2019, pp. 1429–1437. https://doi.org/10.2514/1.G003944.

[5] Gahan, K. C., Hopwood, J. W., and Woolsey, C. A., "Wind Estimate Uncertainty Quantification and Sensitivity Analysis Using Generalized Polynomial Chaos," *Journal of Guidance, Control, and Dynamics*, Vol. 49, No. 3, 2026, pp. 806–818. https://doi.org/10.2514/1.G008513.

[6] Hopwood, J. W., and Woolsey, C. A., "Passivity-based wind estimation for aircraft maneuvering in steady and uniform wind fields," *AIAA SciTech 2024 Forum*, American Institute of Aeronautics and Astronautics, Orlando, FL, 2024, pp. 1–27. https://doi.org/10.2514/6.2024-2654.

[7] Mahapatra, P., and Zrnic, D., "Sensors and systems to enhance aviation safety against weather hazards," *Proceedings of the IEEE*, Vol. 79, No. 9, 1991, pp. 1234–1267. https://doi.org/10.1109/5.97295.

[8] Stratton, D., and Stengel, R., "Real-time decision aiding: aircraft guidance for wind shear avoidance," *IEEE Transactions on Aerospace and Electronic Systems*, Vol. 31, No. 1, 1995, pp. 117–124. https://doi.org/10.1109/7.366298.

[9] Palomaki, R. T., Rose, N. T., van den Bossche, M., Sherman, T. J., and De Wekker, S. F. J., "Wind estimation in the lower atmosphere using multirotor aircraft," *Journal of Atmospheric and Oceanic Technology*, Vol. 34, No. 5, 2017, pp. 1183–1191. https://doi.org/10.1175/JTECH-D-16-0177.1.

[10] Trub, R., Moser, D., Schafer, M., Pinheiro, R., and Lenders, V., "Monitoring meteorological parameters with crowdsourced air traffic control data," *2018 17th ACM/IEEE International Conference on Information Processing in Sensor Networks (IPSN)*, IEEE, Porto, 2018, pp. 25–36. https://doi.org/10.1109/IPSN.2018.00010.

[11] Jacob, J., Chilson, P., Houston, A., and Smith, S., "Considerations for atmospheric measurements with small unmanned aircraft systems," *Atmosphere*, Vol. 9, No. 7, 2018, p. 252. https://doi.org/10.3390/atmos9070252.

[12] Barbieri, L., Kral, S., Bailey, S., Frazier, A., Jacob, J., Reuder, J., Brus, D., Chilson, P., Crick, C., Detweiler, C., Doddi, A., Elston, J., Foroutan, H., González-Rocha, J., Greene, B., Guzman, M., Houston, A., Islam, A., Kemppinen, O., Lawrence, D., Pillar-Little, E., Ross, S., Sama, M., Schmale, D., Schuyler, T., Shankar, A., Smith, S., Waugh, S., Dixon, C., Borenstein, S., and de Boer, G., "Intercomparison of small unmanned aircraft system (sUAS) measurements for atmospheric science during the LAPSE-RATE campaign," *Sensors*, Vol. 19, No. 9, 2019, p. 2179. https://doi.org/10.3390/s19092179.

[13] Adkins, K. A., Akbas, M., and Compere, M., "Real-time urban weather observations for urban air mobility," *International Journal of Aviation, Aeronautics, and Aerospace*, Vol. 7, No. 4, 2020. https://doi.org/10.15394/ijaaa.2020.1540.

[14] Reiche, C., Cohen, A. P., and Fernando, C., "An initial assessment of the potential weather barriers of urban air mobility," *IEEE Transactions on Intelligent Transportation Systems*, Vol. 22, No. 9, 2021, pp. 6018–6027. https://doi.org/10.1109/TITS.2020.3048364.

[15] Thipphavong, D. P., Apaza, R., Barmore, B., Battiste, V., Burian, B., Dao, Q., Feary, M., Go, S., Goodrich, K. H., Homola, J., Idris, H. R., Kopardekar, P. H., Lachter, J. B., Neogi, N. A., Ng, H. K., Oseguera-Lohr, R. M., Patterson, M. D., and Verma, S. A., "Urban air mobility airspace integration concepts and considerations," *2018 Aviation Technology, Integration, and Operations Conference*, American Institute of Aeronautics and Astronautics, Atlanta, GA, 2018, pp. 1–16. https://doi.org/10.2514/6.2018-3676.

[16] Karr, D. A., Wing, D. J., Barney, T. L., Sharma, V., Etherington, T. J., and Sturdy, J. L., "Initial design guidelines for onboard automation of flight path management," *AIAA AVIATION 2021 Forum*, Virtual, 2021, pp. 1–22. https://doi.org/10.2514/6.2021-2326.

[17] González-Rocha, J., Woolsey, C. A., Sultan, C., and De Wekker, S. F. J., "Sensing wind from quadrotor motion," *Journal of Guidance, Control, and Dynamics*, Vol. 42, No. 4, 2019, pp. 836–852. https://doi.org/10.2514/1.G003542.

[18] Halefom, M. H., Hopwood, J. W., and Woolsey, C. A., "Unsteady aerodynamics in model-based wind estimation from fixed-wing aircraft motion," *Journal of Guidance, Control, and Dynamics*, Vol. 47, No. 8, 2024, pp. 1556–1568. https://doi.org/10.2514/1.G007836.

[19] Gahan, K. C., Hopwood, J. W., and Woolsey, C. A., "Model-based wind estimation using H_∞ filtering with flight-test results," *Journal of Guidance, Control, and Dynamics*, Vol. 48, No. 3, 2025, pp. 630–637. https://doi.org/10.2514/1.G007735.

[20] Krener, A. J., "The convergence of the extended Kalman filter," *Directions in Mathematical Systems Theory and Optimization*, Vol. 286, edited by A. Rantzer and C. I. Byrnes, Springer Berlin Heidelberg, Berlin, Heidelberg, 2003, pp. 173–182.

[21] Shim, H., Seo, J. H., and Teel, A. R., "Nonlinear observer design via passivation of error dynamics," *Automatica*, Vol. 39, No. 5, 2003, pp. 885–892. https://doi.org/10.1016/S0005-1098(03)00023-2.

[22] Chen, H., Bai, H., and Taylor, C. N., "Invariant-EKF design for quadcopter wind estimation," *2022 American Control Conference (ACC)*, IEEE, Atlanta, GA, USA, 2022, pp. 1236–1241. https://doi.org/10.23919/ACC53348.2022.9867417.

[23] Ahmed, Z., and Woolsey, C. A., "An Invariant Extended Kalman Filter for Wind Estimation Using a Small, Fixed-Wing Uncrewed

Aerial Vehicle," *IEEE Transactions on Control Systems Technology*, Vol. 33, No. 5, 2025, pp. 1799–1809. https://doi.org/10.1109/TCST.2025.3564884.

[24] Bonnabel, S., Martin, P., and Rouchon, P., "Symmetry-preserving observers," *IEEE Transactions on Automatic Control*, Vol. 53, No. 11, 2008, pp. 2514–2526. https://doi.org/10.1109/TAC.2008.2006929.

[25] Barrau, A., and Bonnabel, S., "The invariant extended Kalman filter as a stable observer," *IEEE Transactions on Automatic Control*, Vol. 62, No. 4, 2017, pp. 1797–1812. https://doi.org/10.1109/TAC.2016.2594085.

[26] Tian, P., Chao, H., Rhudy, M., Gross, J., and Wu, H., "Wind sensing and estimation using small fixed-wing unmanned aerial vehicles: A survey," *Journal of Aerospace Information Systems*, Vol. 18, No. 3, 2021, pp. 132–143. https://doi.org/10.2514/1.I010885.

[27] Ahmed, Z., Halefom, M. H., and Woolsey, C., "Tutorial Review of Indirect Wind Estimation Methods Using Small Uncrewed Air Vehicles," *Journal of Aerospace Information Systems*, Vol. 21, No. 8, 2024, pp. 667–683. https://doi.org/10.2514/1.I011345.

[28] Karagiannis, D., and Astolfi, A., "Nonlinear observer design using invariant manifolds and applications," *Proceedings of the 44th IEEE Conference on Decision and Control*, IEEE, Seville, Spain, 2005, pp. 7775–7780. https://doi.org/10.1109/CDC.2005.1583418.

[29] Hopwood, J., and Woolsey, C., "A symmetry-preserving reduced-order observer," *2025 American Control Conference*, Denver, CO, 2025, pp. 2490–2496. https://doi.org/10.23919/ACC63710.2025.11107972.

[30] Holm, D. D., Schmah, T., and Stoica, C., *Geometric mechanics and symmetry: from finite to infinite dimensions*, Oxford texts in applied and engineering mathematics, Oxford University Press, New York, 2009.

[31] Boothby, W. M., *An Introduction to Differentiable Manifolds and Riemannian Geometry*, revised second ed., Academic Press, San Diego, 2003.

[32] Olver, P. J., *Classical Invariant Theory*, Cambridge University Press, 1999. https://doi.org/10.1017/CBO9780511623660.

[33] Grauer, J. A., and Morelli, E. A., "Generic global aerodynamic model for aircraft," *Journal of Aircraft*, Vol. 52, No. 1, 2015, pp. 13–20. https://doi.org/10.2514/1.C032888.

[34] Hopwood, J. W., Simmons, B. M., Cooper, J. K., and Woolsey, C. A., "Practical Nonlinear Flight Dynamic Modeling for Multirotor Aircraft," *Journal of Aircraft*, 2025, p. Articles in Advance. https://doi.org/10.2514/1.C038103.

[35] Hopwood, J. W., and Woolsey, C. A., "A noise-to-state stable symmetry-preserving reduced-order observer for wind estimation," *AIAA SciTech 2025 Forum*, Orlando, FL, 2025, pp. 1–20. https://doi.org/10.2514/6.2025-1625.

[36] Moylan, P., "A note on Kalman-Bucy filters with zero measurement noise," *IEEE Transactions on Automatic Control*, Vol. 19, No. 3, 1974, pp. 263–264. https://doi.org/10.1109/TAC.1974.1100570.

[37] Gresham, J. L., Fahmi, J.-M. W., Simmons, B. M., Hopwood, J. W., Foster, W., and Woolsey, C. A., "Flight Test Approach for Modeling and Control Law Validation for Unmanned Aircraft," *AIAA SciTech 2022 Forum*, American Institute of Aeronautics and Astronautics, San Diego, CA, 2022, pp. 1–23. https://doi.org/10.2514/6.2022-2406.

[38] Gresham, J. L., "Aerodynamic Modeling in Nonlinear Regions, including Stall Spins, for Fixed-Wing Unmanned Aircraft from Experimental Flight Data," Ph.D. thesis, Virginia Polytechnic Institute and State University, Blacksburg, VA, Mar. 2022.

[39] Simmons, B. M., "Advances in Aero-Propulsive Modeling for Fixed-Wing and eVTOL Aircraft Using Experimental Data," Ph.D. thesis, Virginia Polytechnic Institute and State University, Blacksburg, VA, Apr. 2023.

[40] Simmons, B. M., Gresham, J. L., and Woolsey, C. A., "Aero-propulsive modeling for propeller aircraft using flight data," *Journal of Aircraft*, Vol. 60, No. 1, 2023, pp. 81–96. https://doi.org/10.2514/1.C036773.

[41] Morelli, E. A., "Multiple input design for real-time parameter estimation in the frequency domain," *IFAC Proceedings Volumes*, Vol. 36, No. 16, 2003, pp. 639–644. https://doi.org/10.1016/S1474-6670(17)34833-4.

[42] Morelli, E. A., "Flight-test experiment design for characterizing stability and control of hypersonic vehicles," *Journal of Guidance, Control, and Dynamics*, Vol. 32, No. 3, 2009, pp. 949–959. https://doi.org/10.2514/1.37092.

[43] Morelli, E. A., and Klein, V., *Aircraft System Identification: Theory and Practice*, 2nd ed., Sunflyte Enterprises, Williamsburg, Virginia, 2016.

[44] Morelli, E. A., "Global nonlinear aerodynamic modeling using multivariate orthogonal functions," *Journal of Aircraft*, Vol. 32, No. 2, 1995, pp. 270–277. https://doi.org/10.2514/3.46712.

[45] Simmons, B. M., Gresham, J. L., and Woolsey, C. A., "Flight-test system identification techniques and applications for small, low-cost, fixed-wing aircraft," *Journal of Aircraft*, Vol. 60, No. 5, 2023, pp. 1503–1521. https://doi.org/10.2514/1.C037260.

[46] Rugh, W. J., *Linear system theory*, 2nd ed., Prentice Hall information and system sciences series, Prentice Hall, Upper Saddle River, N.J, 1996.

[47] Khalil, H. K., *Nonlinear Systems*, 3rd ed., Prentice Hall, Upper Saddle Ridge, New Jersey, 2002.